On Azimuthal Resolution of the Lunar-Based SAR Under the Orbital Perturbation Effects

Zhen Xu, *Member, IEEE*, Kun-Shan Chen, *Fellow, IEEE*, and Huadong Guo, *Member, IEEE*

***Abstract*— This article studies the orbital perturbation effects on the azimuthal resolution in lunar-based synthetic aperture radar (LBSAR). We derive explicit expressions for the Doppler frequency modulation rate (DFMR) and beam-crossing velocity using the antenna beam pointing and orbit models. Following that, the azimuthal resolution is expressed in line with orbital elements and synthetic aperture radar (SAR) configurations. The results show that the long-term orbital variations caused by accumulated perturbation effects significantly affect the azimuthal resolution, which, in effect, produces aperiodic variations in the azimuthal resolution. Such a phenomenon is most distinguished for a large LBSAR look angle, leading to a fluctuation of over 30% or even larger in the azimuthal resolution across different cycles. In addition, the errors given rise by short-term orbital perturbations could impact azimuthal resolution to a lesser extent, with corresponding fluctuations consistently below 3%. The findings reveal that it is imperative to consider the irregular variability of azimuthal resolution due to orbital perturbations in the LBSAR.**

***Index Terms*— Azimuthal resolution, beam-crossing velocity, Doppler frequency modulation rate (DFMR), lunar-based synthetic aperture radar (LBSAR), orbital perturbation.**

I. Introduction

EARTH observation from space is typically carried out by sensors erected on low Earth orbit (LEO) satellites [1], [2]. However, the LEO platform poses constraints of sparse viewing and limited revisit time, making it difficult to yield consecutive and seamless coverage of Earth [3], [4], [5]. The lunar-based (LB) platform has the advantages of the enormous swath width, high temporal resolution, and ease of access for installing multisensors [6], [7], [8], [9], [10], [11]. Hence, sensors mounted on the LB platform, particularly the synthetic aperture radar (SAR) [i.e., LB synthetic aperture radar (LBSAR)], are of great potential for Earth observation [12], [13], [14], [15], [16]. The LBSAR can cover most regions of the globe daily and monitor specific areas from several to tens of hours per day if required by applications [17]. These features are attractive for improving Earth observation capabilities, evaluating major natural disasters, and monitoring geodynamics and other emergencies [18]. In this regard, the LBSAR can reinforce our perception of Earth, and thus, it has aroused growing interest from the geoscience and related communities [19], [20], [21], [22], [23], [24], [25], [26], [27], [28], [29].

In SAR configuration parameters, the spatial resolution is crucial for Earth observation, wherein the range resolution of the LBSAR shows little difference with respect to that of the LEOSAR [14]. By contrast, progresses in exploring LBSAR had demonstrated that the unique imaging geometry brings about evident discrepancies in the LBSAR's azimuthal resolution [18], [19], [20], [21]. Nevertheless, little current attention concerning the LBSAR is paid to the azimuthal resolution and its spatiotemporal variation under orbital perturbations though the motion of LBSAR is susceptible to such effects [27], [28], [29].

The satellite, whether natural or artificial, orbiting Earth is affected by perturbation forces, such as terrestrial gravitational perturbation, third-body attraction, and atmospheric drag [30]. These forces could cause temporal variations in the orbital elements and lead to sustained orbital variation and drift, further affecting the SAR movement relative to Earth. In the LEOSAR, orbital perturbations influence little on the Doppler frequency modulation rate (DFMR) and beam-crossing velocity [31]. Correspondingly, the variation in the associated azimuthal resolution is trivial. In the following, as an illustrative example, we analyze the azimuthal resolution of the LEOSAR under conditions of a circular orbit and zero-Doppler centroid that is signified by [32]

$$\rho_a = 0.5\ell_a \cdot V_g V_{\mathrm{SAR}}^{-1} \tag{1}$$

where ℓ_a is the real aperture length, and V_g and V_{SAR} are the beam-crossing velocity and SAR velocity, respectively.

Fig. 1 displays the LEOSAR's azimuthal resolution versus its argument of latitude (AOL) in three consecutive cycles of a perturbed orbit. The relative errors in the azimuthal resolution between each cycle are also presented in Fig. 1. In this case, the LEOSAR is looking from the right-hand side with an incident angle of 45° and an aperture length of 20 m; the platform is orbiting circularly with an altitude of 694.51 km and an orbital inclination of 97.66°. We observe that the LEOSAR could yield a uniform azimuthal resolution that is close to 9.15 m. Between each cycle, the relative error of azimuthal resolution caused by orbital perturbation is negligibly small, indicating that the osculating orbit can be

Manuscript received 2 October 2022; revised 7 February 2023; accepted 7 April 2023. Date of publication 12 April 2023; date of current version 4 May 2023. This work was supported in part by the National Natural Science Foundation of China under Grant 42101398, in part by Shantou University (STU) Scientific Research Foundation for Talents under Grant NTF20023, and in part by the Key Research Program of Frontier Sciences of Chinese Academy of Sciences (CAS) under Grant QYZDY-SSW-DQC026. The work of Kun-Shan Chen was supported by the Initiative Funding of the Guilin University of Technology (GLUT). *(Corresponding author: Kun-Shan Chen.)*

Zhen Xu is with the Department of Electronic and Information Engineering, Shantou University, Shantou 515063, China (e-mail: xuzhen@stu.edu.cn).

Kun-Shan Chen is with the College of Geomatics and Geoinformation, Guilin University of Technology, Guilin 541004, China (e-mail: chenks@glut.edu.cn).

Huadong Guo is with the Aerospace Information Research Institute, Chinese Academy of Sciences, Beijing 100101, China (e-mail: hdguo@radi.ac.cn).

Digital Object Identifier 10.1109/TGRS.2023.3266548

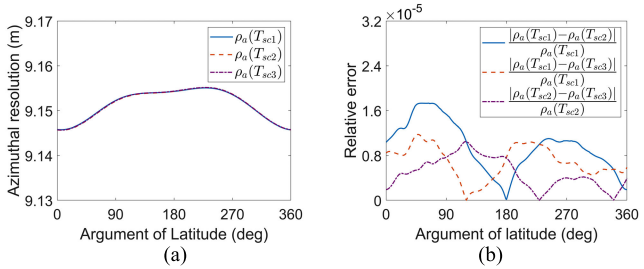

Fig. 1. In three consecutive cycles: (a) azimuth resolution against the AOL and (b) relative error of azimuth resolution between each cycle.

reasonably adopted when it comes to analyzing the LEOSAR's azimuthal resolution.

In the case of LBSAR, (1) is no longer valid due to its imaging geometry and perturbed movement. Specifically, the LBSAR's orbit undergoes considerable orbital perturbations, leading to substantial variation in the Doppler history within the synthetic aperture time (SAT) [27]. As the SAT is far smaller than the cycle of LBSAR orbiting Earth, this effect can be categorized as the short-term orbital perturbation effect. Furthermore, orbital perturbations can be accumulated, leading to continuous and long-term orbital drifts in the LBSAR. As this influence continues throughout the entire mission lifetime of LBSAR, the corresponding effects can be treated as long-term orbital perturbation effects. Under such effects, the orbital inclination of the LBSAR periodically varies between 18.3° and 28.6° with a cycle of 18.6 years, distinguishing it from LEOSAR, whose orbital inclination is generally regarded as time-invariant [29].

From the above arguments, two issues arise: 1) whether the osculating orbit can be used for analyzing LBSAR's azimuthal resolution as it is for LEOSAR and 2) how the azimuthal resolution varies across cycles under accumulated orbital perturbations. This study addresses both issues by deriving the representation of azimuthal resolution and probing into LBSAR's azimuthal resolution variations in various epochs. This article is organized as follows. Section II derives the DFMR and beam-crossing velocity by applying antenna beam pointing and orbital models, further yielding the explicit expression for azimuthal resolution regarding orbital elements and SAR configurations. Following that, Section III theoretically investigates short-term and long-term orbital perturbation effects on azimuthal resolution, showing in detail how orbital variation impacts the azimuthal resolution under both effects. Afterward, Section IV simulates the point target response to illustrate the theoretical analysis. Finally, Section V summarizes the major findings of this study.

II. Representation of the Azimuthal Resolution in the LBSAR

In principle, the azimuthal resolution of an SAR system is defined by [32], [33], [34]

$$\rho_a = V_g \cdot B_D^{-1} \tag{2}$$

with

$$B_D = |f_{\mathrm{DR}}| \cdot T_{\mathrm{SAR}} \tag{2a}$$

where f_{DR} and T_{SAR} are the DFMR and SAT, respectively.

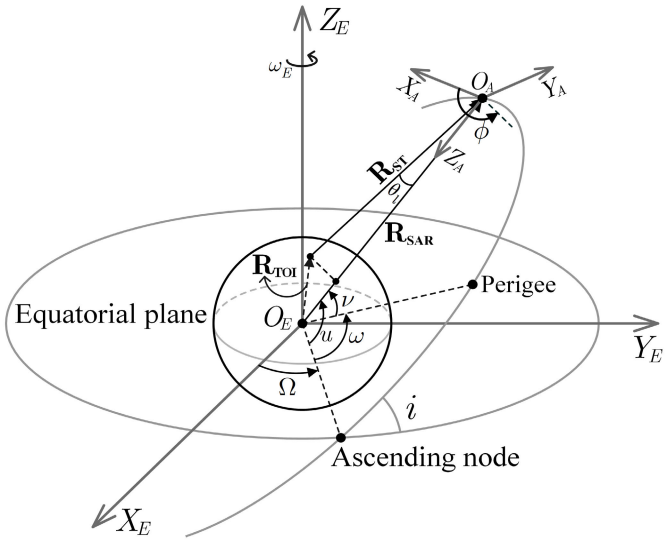

Fig. 2. Observation geometry of LBSAR in the ECI and ACS; the definitions of symbols in the LBSAR geometry are listed in Table I.

TABLE I
Parameters in the Observation Geometry Model of the LBSAR

Symbol	Definitions	Symbol	Definitions
u	Argument of latitude	i	Orbital inclination
ω	Argument of perigee	ν	True anomaly
ω_E	Earth's rotational angular velocity	Ω	Right Ascension of Ascending Node (RAAN)
e	Eccentricity	a	Semi major axis
ϕ	Antenna azimuth angle	θ_l	SAR look angle

As the LBSAR encounters prominent orbital perturbations, its DFMR is sensitive to variations of orbital elements. Besides, the Earth's curvature exhibits great significance in affecting the LBSAR's DFMR due to the extensive spatial coverage; this effect is relevant to the beam-pointing direction in terms of the look and antenna azimuth angles. In what follows, we shall derive the representation of DFMR in line with orbital elements and beam-pointing direction based on the observation geometry shown in Fig. 2.

In the observation geometry, we employ two coordinate systems $O_E - X_E Y_E Z_E$ and $O_A - X_A Y_A Z_A$, i.e., the Earth-centered inertial (ECI) coordinate and the antenna coordinate system (ACS) [24]. Besides, the Moon's orbital elements are provided by the Development Ephemeris 430 (DE430), with the time scale being Barycentric Dynamical Time (TDB) [35], [36], [37], [38]. Note that the signal propagation could lead to a "stop-and-go" error in the LBSAR. Notwithstanding, such an error exerts little impact on the DFMR and azimuthal resolution, as evidenced in [26]. Furthermore, there is no closed-form solution for the Doppler history and associated parameters in the non-stop-and-go echo model [21]. Therefore, the "stop-and-go" assumption is adopted in this study to ascertain orbital perturbation effects on azimuthal resolution.

From [39], the DFMR given rise by the antenna movement relative to the target of interest (TOI) is

$$f_{\mathrm{DR}} = 2\lambda^{-1} \cdot (\Re_1 + \Re_2 + \Re_3 + \Re_4) \tag{3}$$

with

$$\begin{cases} \Re_1 = R_{\mathrm{ST}}^{-1} \cdot (\mathbf{V_{SAR}} \cdot \mathbf{V_{SAR}} + \mathbf{A_{SAR}} \cdot \mathbf{R_{ST}}) \\ \Re_2 = -2R_{\mathrm{ST}}^{-1} \cdot (\mathbf{V_{SAR}} \cdot \mathbf{V_{TOI}}) \\ \Re_3 = R_{\mathrm{ST}}^{-1} \cdot (\mathbf{V_{TOI}} \cdot \mathbf{V_{TOI}} - \mathbf{A_{TOI}} \cdot \mathbf{R_{ST}}) \\ \Re_4 = -R_{\mathrm{ST}}^{-3} \cdot [(\mathbf{V_{SAR}} - \mathbf{V_{TOI}}) \cdot \mathbf{R_{ST}}]^2 \end{cases} \tag{4}$$

where

λ wavelength of the probing signal;
$\mathbf{V_{SAR}}$ SAR velocity vector;
$\mathbf{A_{SAR}}$ SAR acceleration vector;
$\mathbf{V_{TOI}}$ TOI velocity vector due to Earth's rotation;
$\mathbf{A_{TOI}}$ TOI acceleration vector due to Earth's rotation;
$\mathbf{R_{ST}}$ slant range vector that takes the form of

$$\mathbf{R_{ST}} = \mathbf{R_{SAR}} - \mathbf{R_{TOI}} \tag{5}$$

with $\mathbf{R_{SAR}}$ and $\mathbf{R_{TOI}}$ denoting position vectors of the LBSAR and TOI, respectively. Note that the term $\Re_4$ is related to the Doppler centroid f_{dc} by

$$\Re_4 = -0.25R_{\mathrm{ST}}^{-1} \cdot \lambda^2 f_{\mathrm{dc}}^2. \tag{6}$$

By taking account of contributions from the Earth-SAR relative motion, (5) can be further expressed as

$$\Re_4 = \Re_{4\mathrm{S}} + \Re_{4\mathrm{E}} + \Re_{4\mathrm{SE}} \tag{7}$$

where $\Re_{4\mathrm{S}}$ and $\Re_{4\mathrm{E}}$ are correlated with contributions by the SAR motion and Earth's rotation, respectively. The last term $\Re_{4\mathrm{SE}}$ is coupling affected by the SAR motion and Earth's rotation. Their definitions are given by

$$\Re_{4\mathrm{S}} = -R_{\mathrm{ST}}^{3} \cdot (\mathbf{V_{SAR}} \cdot \mathbf{R_{ST}})^2 \tag{8}$$

$$\Re_{4\mathrm{E}} = -R_{\mathrm{ST}}^{-3} \cdot (\mathbf{V_{TOI}} \cdot \mathbf{R_{ST}})^2 \tag{9}$$

$$\Re_{4\mathrm{SE}} = 2R_{\mathrm{ST}}^{-3} \cdot [(\mathbf{V_{SAR}} \cdot \mathbf{R_{ST}}) \cdot (\mathbf{V_{TOI}} \cdot \mathbf{R_{ST}})]. \tag{10}$$

In the above equations, the slant range of the center beam can be expressed by

$$R_{\mathrm{ST}} = \|\mathbf{R_{ST}}\|_2 = R_{\mathrm{SAR}} \cos\theta_l - \sqrt{R_{\mathrm{TOI}}^2 - R_{\mathrm{SAR}}^2 \sin^2\theta_l} \tag{11}$$

where $\|\cdot\|_2$ stands for the ℓ^2-norm product, θ_l is the SAR look angle, and R_{SAR} and R_{TOI} are, respectively, defined as

$$R_{\mathrm{SAR}} = \|\mathbf{R_{SAR}}\|_2 \tag{12}$$

$$R_{\mathrm{TOI}} = \|\mathbf{R_{TOI}}\|_2. \tag{13}$$

For a Keplerian orbit or osculating orbit that is elliptical, the DFMR can be written by

$$f_{\mathrm{DR}}^{\mathrm{kep}} = 2\lambda^{-1} \cdot \left[\left(\Re_1^{\mathrm{kep}} + \Re_{4\mathrm{S}}^{\mathrm{kep}}\right) + \left(\Re_2^{\mathrm{kep}} + \Re_{4\mathrm{SE}}^{\mathrm{kep}}\right) + \left(\Re_3^{\mathrm{kep}} + \Re_{4\mathrm{E}}^{\mathrm{kep}}\right)\right]. \tag{14}$$

In (14), the first parenthesis in the bracket relates to the contribution by SAR motion, with $\Re_1^{\mathrm{kep}}$ and $\Re_{4\mathrm{S}}^{\mathrm{kep}}$, respectively, expressed by

$$\Re_1^{\mathrm{kep}} = -\mu \cdot R_{\mathrm{SAR}}^{-2} \cdot \cos\theta_l + R_{\mathrm{ST}}^{-1} V_{\mathrm{kep}}^2 \cdot \left(1 + e^2 + 2e\cos v\right) \tag{15}$$

$$\begin{aligned} \Re_{4\mathrm{S}}^{\mathrm{kep}} = & -R_{\mathrm{ST}}^{-1} V_{\mathrm{kep}}^2 \cdot [2e(e\cos\nu + 1) \cdot \sin\nu \sin\theta_l \cos\theta_l \cos\phi \\ & + (1 + e\cos\nu)^2 \cdot \cos^2\theta_l \\ & + e^2 \cdot \sin^2\nu \cdot \sin^2\theta_l \cdot \cos^2\phi]. \end{aligned} \tag{16}$$

The second term in (14) is coupling influenced by the SAR motion and Earth's rotation, which can be written as

$$\begin{aligned} \Re_2^{\mathrm{kep}} = & -2R_{\mathrm{ST}}^{-1} \cdot \omega_E \cdot V_{\mathrm{kep}} \\ & \cdot \{(e\cos\nu + 1) \cdot [(R_{\mathrm{SAR}} - R_{\mathrm{ST}}\cos\theta_l)\cos i \\ & - R_{\mathrm{ST}} \sin\theta_l \sin\phi \sin i \sin u] \\ & + e \cdot R_{\mathrm{ST}} \sin\theta_l \sin\nu \\ & \cdot (-\cos\phi\cos i + \sin\phi \sin i \cos u)\} \end{aligned} \tag{17}$$

$$\begin{aligned} \Re_{4\mathrm{SE}}^{\mathrm{kep}} = & -2\omega_E R_{\mathrm{SAR}} R_{\mathrm{ST}}^{-1} \\ & \cdot V_{\mathrm{kep}} \cdot \sin\theta_l \cdot (\sin\phi \sin i \cos u - \cos\phi\cos i) \\ & \cdot [(e\cos\nu + 1) \cdot \sin\theta_l \cos\phi + e\sin\nu\cos\theta_l]. \end{aligned} \tag{18}$$

The third term of the DFMR is dependent on Earth's rotation only, and each component takes the form of

$$\begin{aligned} \Re_3^{\mathrm{kep}} = & R_{\mathrm{ST}}^{-1}\omega_E^2 \\ & \cdot \{R_{\mathrm{SAR}}^2 - R_{\mathrm{SAR}} R_{\mathrm{ST}} \cos\theta_l \\ & + R_{\mathrm{SAR}} \sin^2 i \sin^2 u (R_{\mathrm{ST}}\cos\theta_l - R_{\mathrm{SAR}}) \\ & - R_{\mathrm{SAR}} R_{\mathrm{ST}} \sin\theta_l \sin i \sin u \\ & \times (\cos\phi \sin i \cos u + \sin\phi \cos i)\} \end{aligned} \tag{19}$$

$$\begin{aligned} \Re_{4\mathrm{E}}^{\mathrm{kep}} = & -\omega_E^2 R_{\mathrm{SAR}}^2 R_{\mathrm{ST}}^{-1} \sin^2\theta_l \\ & \cdot (\sin^2\phi \sin^2 i \cos^2 u \\ & + \cos^2\phi\cos^2 i - 2\sin\phi\cos\phi \\ & \cdot \sin i \cos i \cos u) \end{aligned} \tag{20}$$

with

$$V_{\mathrm{kep}} = \sqrt{\mu \cdot a^{-1} \cdot (1 - e^2)^{-1}} \tag{21}$$

where μ is the gravitational coefficient of the Earth.

For the perturbed orbit, the DFMR of the SAR system is modified to

$$f_{\mathrm{DR}}^{\mathrm{per}} = 2\lambda^{-1} \cdot \left[\left(\Re_1^{\mathrm{per}} + \Re_{4\mathrm{S}}^{\mathrm{per}}\right) + \left(\Re_2^{\mathrm{per}} + R_{4\mathrm{SE}}^{\mathrm{per}}\right) + \left(\Re_3^{\mathrm{per}} + R_{4\mathrm{E}}^{\mathrm{per}}\right)\right] \tag{22}$$

with

$$\begin{aligned} \Re_1^{\mathrm{per}} = & R_{\mathrm{ST}}^{-1} \cdot \left(\mathbf{V_{SAR}^{ECI}} \cdot \mathbf{V_{SAR}^{ECI}}\right) - A_x^{\mathrm{ACS}} \sin\theta_l \cos\phi \\ & + A_y^{\mathrm{ACS}} \sin\theta_l \sin\phi - A_z^{\mathrm{ACS}} \cos\theta_l \end{aligned} \tag{23}$$

$$\begin{aligned} \Re_{4\mathrm{S}}^{\mathrm{per}} = & -R_{\mathrm{ST}}^{-1} \cdot \left[\left(V_x^{\mathrm{ACS}}\right)^2 \sin^2\theta_l \cos^2\phi \right. \\ & + \left(V_z^{\mathrm{ACS}}\right)^2 \cos^2\theta_l \\ & \left. + 2V_x^{\mathrm{ACS}} \cdot V_z^{\mathrm{ACS}} \sin\theta_l \cos\theta_l \cos\phi\right] \end{aligned} \tag{24}$$

$$\begin{aligned} \Re_2^{\mathrm{per}} = & -2R_{ST}^{-1} \cdot \omega_E \\ & \cdot \{V_x^{\mathrm{ACS}} \cdot [(R_{\mathrm{SAR}} - R_{\mathrm{ST}}\cos\theta_l)\cos i \\ & - R_{\mathrm{ST}} \sin\theta_l \sin\phi \sin i \sin u] \\ & - V_z^{\mathrm{ACS}} (R_{\mathrm{ST}} \sin\theta_l \cos\phi \cos i \\ & - R_{\mathrm{ST}} \sin\theta_l \sin\phi \sin i \cos u)\} \end{aligned} \tag{25}$$

$$\begin{aligned} \Re_{4\mathrm{SE}}^{\mathrm{per}} = & -2\omega_E R_{\mathrm{SAR}} R_{\mathrm{ST}}^{-1} \cdot \sin\theta_l \cdot (\sin\phi \sin i \cos u \\ & - \cos\phi\cos i) \cdot \left(V_x^{\mathrm{ACS}} \cdot \sin\theta_l \cos\phi + V_z^{\mathrm{ACS}} \cos\theta_l\right) \end{aligned} \tag{26}$$

$$\Re_3^{\mathrm{per}} = \Re_3^{\mathrm{kep}} \tag{27}$$

$$\Re_{4\mathrm{E}}^{\mathrm{per}} = \Re_{4\mathrm{E}}^{\mathrm{kep}}. \tag{28}$$

It is noteworthy that expressions of $\Re_3$ and $\Re_{4E}$ remain the same with and without orbital perturbations, as both terms are correlated with Earth's rotation only. In (23)–(26), the vectors $\mathbf{V}_{\mathbf{SAR}}^{\mathbf{ACS}} = [V_x^{\mathrm{ACS}}, V_y^{\mathrm{ACS}}, V_z^{\mathrm{ACS}}]^T$ and $\mathbf{A}_{\mathbf{SAR}}^{\mathbf{ACS}} = [A_x^{\mathrm{ACS}}, A_y^{\mathrm{ACS}}, A_z^{\mathrm{ACS}}]^T$ are LBSAR's velocity and acceleration vectors in the ACS. The other two related vectors are the LBSAR's velocity and acceleration vectors in the ECI, which are, respectively, denoted by $\mathbf{V}_{\mathbf{SAR}}^{\mathbf{ECI}} = [V_x^{\mathrm{ECI}}, V_y^{\mathrm{ECI}}, V_z^{\mathrm{ECI}}]^T$ and $\mathbf{A}_{\mathbf{SAR}}^{\mathbf{ECI}} = [A_x^{\mathrm{ECI}}, A_y^{\mathrm{ECI}}, A_z^{\mathrm{ECI}}]^T$. The transformations of those two vectors from the ECI coordinate to the ACS are given by

$$\begin{cases} V_x^{\mathrm{ACS}} = -V_x^{\mathrm{ECI}} \cdot (\sin u \cos \Omega + \cos i \cos u \sin \Omega) \\ \qquad\qquad - V_y^{\mathrm{ECI}} \cdot (\sin u \sin \Omega - \cos i \cos u \cos \Omega) \\ \qquad\qquad + V_z^{\mathrm{ECI}} \cdot \sin i \cos u \\ V_y^{\mathrm{ACS}} = -V_x^{\mathrm{ECI}} \cdot \sin i \sin \Omega + V_y^{\mathrm{ECI}} \cdot \sin i \cos \Omega - V_z^{\mathrm{ECI}} \cdot \cos i \\ V_z^{\mathrm{ACS}} = -V_x^{\mathrm{ECI}} \cdot (\cos u \cos \Omega - \cos i \sin u \sin \Omega) \\ \qquad\qquad - V_y^{\mathrm{ECI}} \cdot (\cos u \sin \Omega + \cos i \sin u \cos \Omega) \\ \qquad\qquad + V_z^{\mathrm{ECI}} \cdot \sin i \sin u \end{cases} \tag{29}$$

$$\begin{cases} A_x^{\mathrm{ACS}} = -A_x^{\mathrm{ECI}} \cdot (\sin u \cos \Omega + \cos i \cos u \sin \Omega) \\ \qquad\qquad - A_y^{\mathrm{ECI}} \cdot (\sin u \sin \Omega - \cos i \cos u \cos \Omega) \\ \qquad\qquad + A_z^{\mathrm{ECI}} \cdot \sin i \cos u \\ A_y^{\mathrm{ACS}} = -A_x^{\mathrm{ECI}} \cdot \sin i \sin \Omega + A_y^{\mathrm{ECI}} \cdot \sin i \cos \Omega - A_z^{\mathrm{ECI}} \cdot \cos i \\ A_z^{\mathrm{ACS}} = -A_x^{\mathrm{ECI}} (\cos u \cos \Omega - \cos i \sin u \sin \Omega) \\ \qquad\qquad - A_y^{\mathrm{ECI}} (\cos u \sin \Omega + \cos i \sin u \cos \Omega) \\ \qquad\qquad - A_z^{\mathrm{ECI}} \cdot \sin i \sin u. \end{cases} \tag{30}$$

Note that, in the lunar ephemeris of DE430, the position and velocity vectors of the Moon's barycenter are provided in the ECI coordinate, but the acceleration vector is unavailable. Thus, the corresponding acceleration is obtained numerically by the DE430.

Now, we consider the beam-crossing velocity. In the LBSAR, Earth's rotation dominates the beam-crossing velocity, while the contribution from SAR motion is relatively small. Thus, the beam-crossing velocity under the Keplerian and perturbed orbits are, respectively, given by

$$V_g^{\mathrm{kep}} = \left\| \mathbf{V}_{\mathbf{TOI}}^{\mathbf{ACS}} - \mathbf{p} \cdot V_{\mathrm{kep}} \left(1 - R_{\mathrm{ST}} R_{\mathrm{SAR}}^{-1} \cos \theta_l\right) \right\|_2 \tag{31}$$

$$\mathbf{p} = [1 + e \cos \nu, 0, -e \sin \nu]^T \tag{32}$$

and

$$V_g^{\mathrm{per}} = \left\| \mathbf{V}_{\mathbf{TOI}}^{\mathbf{ACS}} - \mathbf{V}_{\mathbf{SAR}}^{\mathbf{ACS}} \cdot (1 - R_{\mathrm{ST}} R_{\mathrm{SAR}}^{-1} \cos \theta_l) \right\|_2. \tag{33}$$

In (31) and (32), the vector $\mathbf{V}_{\mathbf{TOI}}^{\mathbf{ACS}}$ in the ACS, defined as the TOI's linear velocity vector given rise by Earth's rotation, is expressed as (34), shown at the bottom of the next page. Derivations of the above equations are given in the Appendix.

In the SAR system, the SAT depends on its imaging mode. According to Fornaro et al. [18], the LBSAR operates equivalently in the sliding spotlight mode with a specified real aperture length along the azimuthal direction. However, this mode demands a vast aperture and leads to nonuniform azimuthal resolution within the image scene of the LBSAR [20], which is highly undesirable for most applications. Thus, the sliding spotlight mode perhaps is not the priority in the LBSAR in many aspects of Earth observation.

The coherent processing of the LBSAR can be independent of the aperture antenna but relies only on the synthetic angle. This mode is identical to the spotlight mode, which is also widely applied in the planetary radars [40], [41]. In this mode, the azimuthal resolutions with and without orbital perturbation effects, respectively, take the forms of

$$\rho_a^{\mathrm{per}} = 0.5 \cdot \lambda \Big/ \theta_{\mathrm{syn}}^{\mathrm{per}} \tag{35}$$

$$\theta_{\mathrm{syn}}^{\mathrm{per}} = 0.5\lambda \cdot \left| f_{\mathrm{DR}}^{\mathrm{per}} \right| \cdot T_{\mathrm{SAR}} \Big/ V_g^{\mathrm{per}} \tag{36}$$

and

$$\rho_a^{\mathrm{kep}} = 0.5 \cdot \lambda \Big/ \theta_{\mathrm{syn}}^{\mathrm{kep}} \tag{37}$$

$$\theta_{\mathrm{syn}}^{\mathrm{kep}} = 0.5\lambda \cdot \left| f_{\mathrm{DR}}^{\mathrm{kep}} \right| \cdot T_{\mathrm{SAR}} \Big/ V_g^{\mathrm{kep}}. \tag{38}$$

The spotlight mode allows for constructing the antenna without considering the azimuthal resolution and real aperture length. Furthermore, the LBSAR in the spotlight mode can provide relatively uniform azimuthal resolution for most covered regions, as evidenced in the following. Preliminary analysis shows that an SAT within the range of 100–200 s is suitable for Earth observation when the L-band LBSAR is employed [17], [24], [25], [26], [27], [28], [29]. Hence, in this study, the LBSAR works in spotlight mode with an SAT of 200 s and a carrier frequency of 1.2 GHz.

So far, we have derived representations of the DFMR, beam-crossing velocity, and associated azimuthal resolutions in both Keplerian and perturbed orbits. One critical issue in the LBSAR concerns the orbital perturbation effects on azimuthal resolution, and the detailed analysis concerning such effects is presented in Section III.

III. Evaluations of the Orbital Perturbation Effects on the LBSAR Azimuthal Resolution

The analysis regarding the effects of orbital perturbations on the azimuthal resolution can be divided into two categories: short- and long-term orbital perturbations. The former manifests as the change of azimuthal resolution within the SAT, which is more concerned with evaluating the imaging performance of the LBSAR. In contrast, the latter considers variations in LBSAR's azimuthal resolutions across different cycles. This effect is caused by long-term accumulated orbital perturbation, and it is crucial for the secular Earth observation by the LBSAR. The changes in azimuthal resolution induced by short-term orbital perturbations are first discussed in the following.

A. Azimuthal Resolution of the LBSAR Under Short-Term Orbital Perturbation Effects

To evaluate the short-term orbital perturbation effects on the LBSAR's azimuthal resolution, we assume that the perturbed orbit intersects with the osculating one at zero-azimuth time. With this assumption, a relative error concerning the azimuthal resolution variation within the SAT can be defined as

$$\delta_{ar} = \left(\rho_a^{\mathrm{per}} - \rho_a^{\mathrm{kep}}\right) \Big/ \rho_a^{\mathrm{per}}. \tag{39}$$

TABLE II
EPOCHS FOR VARIOUS CYCLES OF THE LBSAR IN TDB AND CORRESPONDING SCOPES OF ORBITAL ELEMENTS

Cycle	Corresponding epoch in TDB	AOL	Orbital Inclination	RAAN	Earth-LBSAR distance
$T_{\text{LC\_1}}$	From 05:05:29.07, Mar. 11, 2024 to 16:13:49.76, Apr. 07, 2024	0°~360°	28.52°~28.58°	2.90°~2.93°	3.58×10^8 m~4.06×10^8 m
$T_{\text{LC\_2}}$	From 16:13:49.76, Apr. 07, 2024 to 01:31:58.56, May. 05, 2024	0°~360°	28.52°~28.57°	2.84°~2.92°	3.59×10^8 m~4.06×10^8 m
$T_{\text{LC\_3}}$	From 01:31:58.56, May. 05, 2024 to 07:59:53.05, Jun. 01, 2024	0°~360°	28.42°~28.52°	2.54°~2.85°	3.63×10^8 m~4.05×10^8 m
$T_{\text{LC\_4}}$	From 18:22:18.15, Jun. 19, 2033 to 01:06:30.68, Jul. 17, 2033	0°~360°	18.61°~18.71°	355.09°~355.83°	3.68×10^8 m~4.04×10^8 m
$T_{\text{LC\_5}}$	From 01:06:30.68, Jul. 17, 2033 to 09:15:05.52, Aug. 13, 2033	0°~360°	18.47°~18.62°	355.82°~356.37°	3.63×10^8 m~4.05×10^8 m
$T_{\text{LC\_6}}$	From 09:15:05.52, Aug. 13, 2033 to 19:12:26.04, Sep. 09, 2033	0°~360°	18.33°~18.47°	356.35°~356.56°	3.59×10^8 m~4.06×10^8 m
$T_{\text{LC\_7}}$	From 06:08:25.55, Sep. 29, 2042 to 17:16:34.61, Oct. 26, 2042	0°~360°	28.43°~28.51°	3.08°~3.29°	3.57×10^8 m~4.06×10^8 m
$T_{\text{LC\_8}}$	From 17:16:34.61, Oct. 26, 2042 to 02:32:55.59, Nov. 23, 2042	0°~360°	28.33°~28.43°	2.61°~3.08°	3.60×10^8 m~4.05×10^8 m
$T_{\text{LC\_9}}$	From 02:32:55.59, Nov. 23, 2042 to 08:40:11.77, Dec. 20, 2042	0°~360°	28.32°~28.40°	2.04°~2.61°	3.65×10^8 m~4.05×10^8 m

By taking account of (35)–(38), (39) can be simplified to

$$\delta_{ar} = 1 - (1 - \delta_{dr})^{-1} \cdot (1 - \delta_{gv}) \tag{40}$$

with

$$\delta_{dr} = \left(f_{\text{DR}}^{\text{per}} - f_{\text{DR}}^{\text{kep}}\right) \Big/ f_{\text{DR}}^{\text{per}} \tag{41}$$

$$\delta_{gv} = \left(V_g^{\text{per}} - V_g^{\text{kep}}\right) \Big/ V_g^{\text{per}}. \tag{42}$$

As indicated in (40)–(42), the relative error of azimuthal resolution δ_{ar} is correlated with δ_{dr} and δ_{gv} being the relative errors of the DFMR and beam-crossing velocity. In other words, the short-term orbital perturbations separately impact the DFMR and beam-crossing velocity, leading to diverse variations in the azimuthal resolution.

To illustrate the phenomenon mentioned above, the relative errors δ_{ar}, δ_{dr}, and δ_{gv} are drawn in Fig. 3 as a function of the look angle, respectively. To be consistent with studies in [27], [28], and [29], and without loss of generality, the zero-azimuth time is set to 00:00:00 on March 20, 2024, TDB. In addition, the LBSAR is left-looking with a near-look angle of 0.2° and a beamwidth of 0.6°, while the antenna azimuth angle is regulated by the zero Doppler steering method proposed in [25].

Fig. 3 demonstrates that the relative error δ_{dr} decreases as the LBSAR's look angle increases. As for the relative error of beam-crossing velocity, it is seen to descend with increasing look angle until about 0.78°. Beyond this scope, the relative error ascends slightly. In addition, the variation magnitude of beam-crossing velocity is smaller than that of the DFMR. As a result, an incremental relative error followed by the increasing look angle appears in the LBSAR's azimuthal resolution. Furthermore, the magnitude of δ_{ar} remains below 0.02, suggesting that the azimuthal resolution of the LBSAR is not significantly affected by the short-term orbital perturbations.

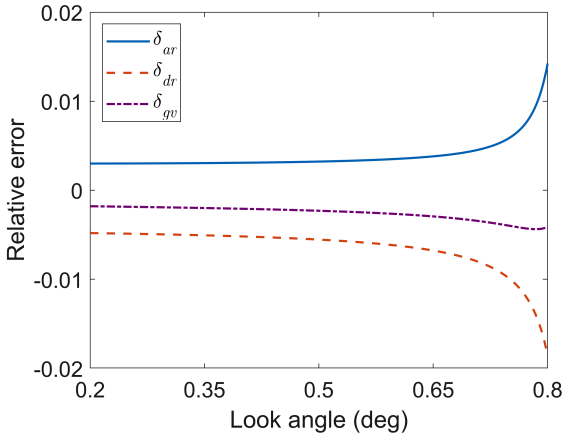

Fig. 3. Relative errors of the azimuthal resolution, DFMR, and beam-crossing velocity versus the LBSAR look angle.

Next, the short-term orbital perturbation effects on the azimuthal resolution of the LBSAR at specified locations in various cycles are further checked for a more rigorous analysis. Two extreme cases are considered: the maximal and minimal orbital inclinations; under both cases, various cycles orbiting the Earth are taken into account. Table II lists the epochs in the TDB corresponding to these cycles and summarizes the scopes of orbital elements within these epochs.

By the same argument as in Fig. 3, the orbital elements with and without short-term orbital perturbations are assumed to be the same at the zero-azimuth time. With this assumption, Fig. 4 presents the relative error δ_{ar} against the look angle at different AOLs over three consecutive cycles, i.e., $T_{\text{LC\_1}}$~$T_{\text{LC\_3}}$, when the LBSAR's orbital inclination approaches its maximum magnitude. In this simulation, the location of the LBSAR is signified by u_0, the AOL at the zero-azimuth time.

Fig. 4 illustrates that there are various relative errors δ_{ar} in different cycles; also, different locations correspond to

$$\mathbf{V}_{\text{TOI}}^{\text{ACS}} = \omega_E \begin{bmatrix} (R_{\text{SAR}} - R_{\text{ST}}\cos\theta_l)\cos i - R_{\text{ST}}\sin\theta_l \sin\phi \sin i \sin u \\ (R_{\text{SAR}} - R_{\text{ST}}\cos\theta_l)\sin i \cos u - R_{\text{ST}}\sin\theta_l \cos\phi \sin i \sin u \\ -R_{\text{ST}}\sin\theta_l \sin\phi \sin i \cos u + R_{\text{ST}}\sin\theta_l \cos\phi \cos i \end{bmatrix}. \tag{34}$$

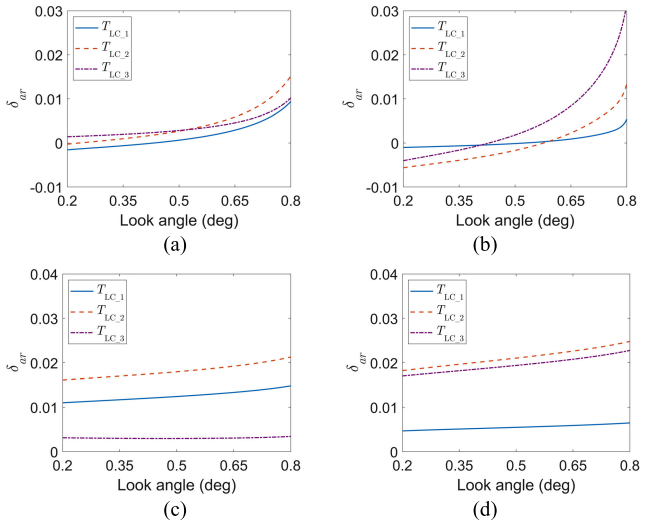

Fig. 4. In cycles $T_{\text{LC\_1}}\sim T_{\text{LC\_3}}$, the relative error of azimuthal resolution versus look angle of the LBSAR at locations of (a) $u_0 = 60°$, (b) $u_0 = 90°$, (c) $u_0 = 240°$, and (d) $u_0 = 270°$.

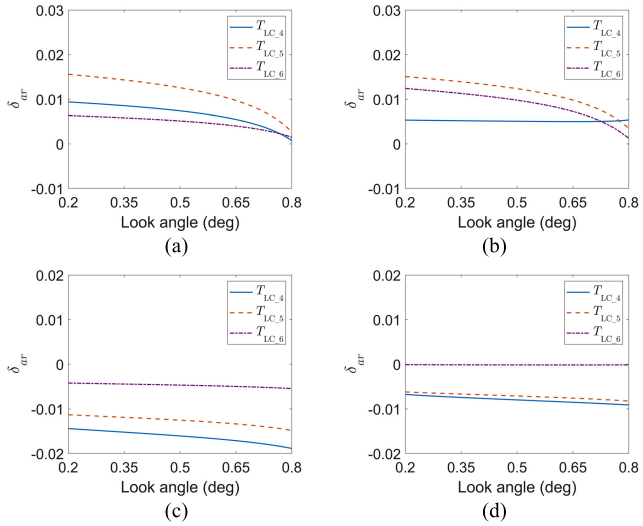

Fig. 5. In cycles $T_{\text{LC\_4}}\sim T_{\text{LC\_6}}$, the relative error of azimuthal resolution versus look angle of the LBSAR at locations of (a) $u_0 = 60°$, (b) $u_0 = 90°$, (c) $u_0 = 240°$, and (d) $u_0 = 270°$.

different relative errors in azimuth resolution. Accordingly, the short-term orbital perturbation exerts distinct effects on the LBSAR's azimuthal resolution depending on its location and cycle. Moreover, the magnitude of δ_{ar} is quite limited though it shows a broad uptrend versus the LBSAR's look angle. One can conclude that the short-term orbital perturbation exhibits only trivial impacts on influencing the azimuthal resolution when the orbital inclination of LBSAR is large.

We now examine the azimuthal resolution changes induced by the short-term orbital perturbation under the small orbital inclination condition by selecting cycles $T_{\text{LC\_4}}\sim T_{\text{LC\_6}}$. In these cycles, the relative errors δ_{ar} against the look angle at various AOLs are presented in Fig. 5. Interestingly, the relative error of azimuthal resolution shows a downward trend with respect to the look angle for most conditions. Besides, the magnitudes of relative errors are consistently smaller than 0.02 though their changes are diverse for different AOLs and cycles. Hence, the short-term orbital perturbation has little bearing on the LBSAR azimuthal resolution under a small orbital inclination condition.

Figs. 3–5 reveals that the short-term orbital perturbations could affect the LBSAR's azimuthal resolution, but to a small extent. The findings also hold for other locations and cycles in LBSAR. The rationale behind this phenomenon is that Earth's rotation, the predominant factor in determining the LBSAR's DFMR and beam-crossing velocity, is approximately independent of the short-term orbital perturbation. In contrast, the LBSAR motion plays a minor role in affecting azimuthal resolution though it is susceptible to short-term orbital perturbation. Therefrom, compared to the osculating orbit, the orbital perturbations within the SAT only bring about a variety of slight variations to the azimuthal resolution of the LBSAR. Nevertheless, once the long periodical variations of elements are considered, the influences on the LBSAR's azimuthal resolution subjected to long-term orbital perturbations are particularly considerable, as discussed in the following.

B. Azimuthal Resolution of the LBSAR Under Long-Term Orbital Perturbation Effects

In the LBSAR, the long-term orbital perturbations and their effects on the azimuthal resolution are more deserving of attention, as the location of TOI relative to LBSAR could be affected by such effects. Significantly, there are diversities of relative locations between the TOI and LBSAR in different cycles for a specified beam-pointing direction (e.g., pointing to the zero-Doppler plane). To provide a detailed description, we define two geographical coordinate errors that correlate to the relative location between the TOI and SAR in the ECI coordinate

$$\delta_\Lambda = \Lambda_{\text{TOI}} - \Lambda_{\text{SNP}} \tag{43}$$

$$\delta_\Phi = \Phi_{\text{TOI}} - \Phi_{\text{SNP}} \tag{44}$$

where Λ_{TOI} and Φ_{TOI} are the TOI's longitude and latitude, and Λ_{SNP} and Φ_{SNP} are the SAR nadir point's longitude and latitude.

In Fig. 6, the geographical coordinate errors of the LBSAR over three consecutive cycles ($T_{\text{LC\_1}}\sim T_{\text{LC\_3}}$) are plotted as a function of the AOL. For comparison, the errors δ_Λ and δ_Φ of the LEOSAR versus the AOL are also shown in Fig. 6 using the LEOSAR's configurations depicted in Fig. 1.

From Fig. 6, it is observed that the TOI's location relative to SAR varies with the varying AOL; the corresponding variation regularities depend on the platform. In the case of LEOSAR, the relative locations of TOI remain roughly the same across different cycles. By comparison, both δ_Λ and δ_Φ correspond to discrepant variation features in different cycles of the LBSAR due to long-term orbital perturbations. As a result, Earth's rotation, which dominates the LBSAR's azimuthal resolution, varies conspicuously over different cycles. Therefore, it is crucial to examine variations in the LBSAR's azimuthal resolution across different cycles due to the remarkable influences of long-term orbital perturbations.

To assist in inspecting the long-term orbital perturbation effects on the LBSAR's azimuthal resolution, a relative error concerning its fluctuation across two different cycles is defined

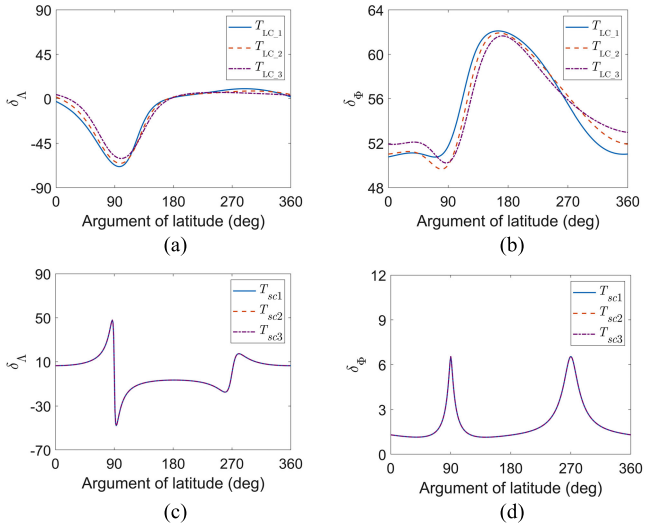

Fig. 6. In three consecutive cycles, the geographical coordinate errors in LBSAR: (a) δ_Λ versus the AOL and (b) δ_Φ versus the AOL; the geographical coordinate errors in LEOSAR: (c) δ_Λ versus the AOL and (d) versus the AOL.

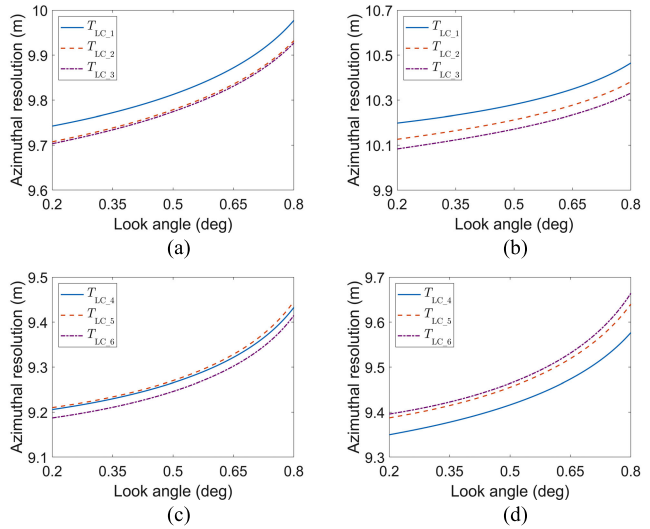

Fig. 7. In the LBSAR, the azimuthal resolution versus the look angle in cycles $T_{\mathrm{LC\_1}}\sim T_{\mathrm{LC\_3}}$ at the AOL of (a) 240° and (b) 270°; the azimuthal resolution versus the look angle in cycles $T_{\mathrm{LC\_4}}\sim T_{\mathrm{LC\_6}}$ at the AOL of (c) 240° and (d) 270°.

as follows:

$$\Delta_{\mathrm{az\_mn}}(u_0) = \frac{\rho_a^{\mathrm{per}}(u_0, T_{\mathrm{LC\_m}}) - \rho_a^{\mathrm{per}}(u_0, T_{\mathrm{LC\_}n})}{\rho_a^{\mathrm{per}}(u_0, T_{\mathrm{LC\_}m})} \times 100\% \tag{45}$$

where $m, n = 1, \ldots, 9$; $m \neq n$, $\rho_a^{\mathrm{per}}(u_0, T_{\mathrm{LC\_m}})$, and $\rho_a^{\mathrm{per}}(u_0, T_{\mathrm{LC\_}n})$, respectively, represent the azimuthal resolutions of the LBSAR at the AOL of u_0 in the cycles $T_{\mathrm{LC\_}m}$ and $T_{\mathrm{LC\_}n}$. One cycle of LBSAR corresponds to the AOL ranging from 0° to 360°.

First, we examine the relevant relationship between the azimuthal resolutions and look angle in different LBSAR cycles. By so doing, Fig. 7(a) and (b) draws the azimuthal resolution versus look angle at the AOLs of 240° and 270° in cycles $T_{\mathrm{LC\_1}}\sim T_{\mathrm{LC\_3}}$. For comparison, Fig. 7(c) and (d) plots the azimuthal resolution against the look angle at the same AOLs in cycles $T_{\mathrm{LC\_4}}\sim T_{\mathrm{LC\_6}}$.

It can be identified from Fig. 7 that the azimuthal resolution shows a general tendency to be coarser with an increasing look angle in the LBSAR. By comparing Fig. 7(a) and (b) with Fig. 7(c) and (d), we see that azimuthal resolution is higher under the same LBSAR configurations when the orbital inclination condition is small. Overall, the azimuthal resolution is uniform for most of the regions covered by the LBSAR. Such properties, which are strongly desirable for Earth observation, can be attainable in the LBSAR by employing the spotlight mode.

To put forward a comprehensive analysis of the azimuthal resolution under long-term orbital perturbations in the LBSAR, Fig. 8(a)–(c) presents the azimuthal resolutions with various look angles against AOL in cycles $T_{\mathrm{LC\_1}}\sim T_{\mathrm{LC\_3}}$. Besides, the associated relative errors of azimuthal resolution between each cycle are presented in Fig. 8(d)–(e) as a function of AOL.

Fig. 8 illustrates that the azimuthal resolution has valley and peak values at the AOLs of 0° and around 90°, respectively. Afterward, the azimuthal resolution exhibits a downward trend with regard to the increasing AOL. At around 180° of the AOL, the azimuthal resolution reaches its local minimum. This pattern repeats within the range of AOL from 180° to 360°. Besides, the variations in azimuthal resolutions are closely related to the look angle of the LBSAR. For a look angle of 0.8°, the difference in azimuthal resolution between one cycle to another is substantial, with a maximal fluctuation being up to 32%. Moreover, the peak locations of the azimuthal resolution fluctuations are in close proximity to those of azimuthal resolutions. Regarding the look angles of 0.2° and 0.5°, fluctuations across different cycles are persistently below 3%, suggesting that there are minor differences in azimuthal resolutions between each cycle. Within the AOL ranging from 180° to 360°, the azimuthal resolutions show lesser differences even for a large look angle, implying that the LBSAR's azimuthal resolution is homogeneous in this case.

It is desirable to inspect long-term variation of azimuthal resolution under the small orbital inclination condition. Thus, Fig. 9(a)–(c) presents the azimuthal resolutions with various look angles against AOL in cycles $T_{\mathrm{LC\_4}}\sim T_{\mathrm{LC\_6}}$. To facilitate comparison, the relative errors concerning fluctuations of the LBSAR's azimuthal resolution across those cycles are plotted in Fig. 9(d)–(f) against the AOL.

As shown in Fig. 9, there are two peaks and three dips in the variation curve of azimuthal resolution regarding AOL, which are similar to trends shown in Fig. 8. However, comparisons of Figs. 8 and 9 reveal the first peak of the variation curve shrank sharply for a look angle of 0.8°. Also, the differences in azimuthal resolutions between each cycle lessen in this event, with fluctuations persistently below 5%. Correspondingly, the LBSAR could yield a more uniform and finer azimuthal resolution when the orbital inclination is small. Another finding rests with shifting peak locations of azimuthal resolution's variation curves in different cycles, which is most evident for a look angle of 0.8°: the first peak of the variation curve locates at the AOL around 114° in cycle $T_{\mathrm{LC\_4}}$, while it migrates to the AOL of 95° in cycle $T_{\mathrm{LC\_6}}$. Interestingly, the peak locations of relative errors are no longer close to those of azimuthal resolutions. Hence, long-term orbital

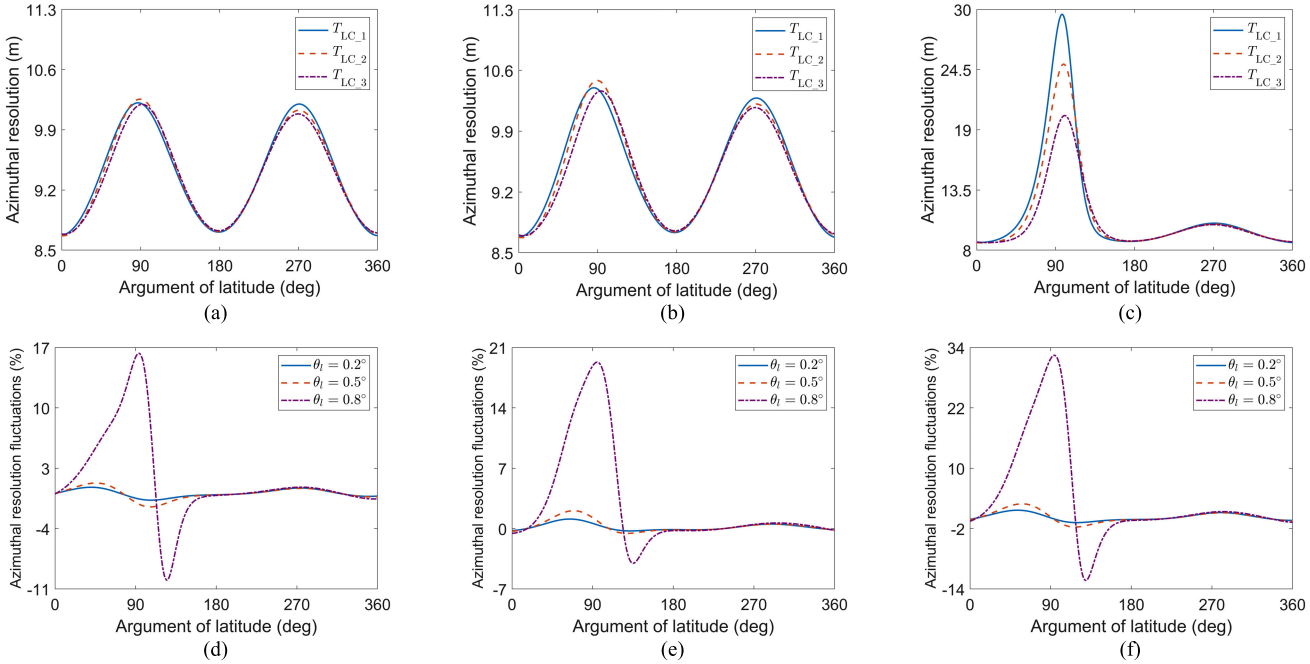

Fig. 8. In cycles T_{LC_1}∼T_{LC_3}, the azimuthal resolution versus the AOL of the LBSAR with look angles of (a) 0.2°, (b) 0.5°, and (c) 0.8°. The relative errors with various look angles versus the AOL, where (d) is Δ_{az_12}, (e) is Δ_{az_23}, and (f) is Δ_{az_13}.

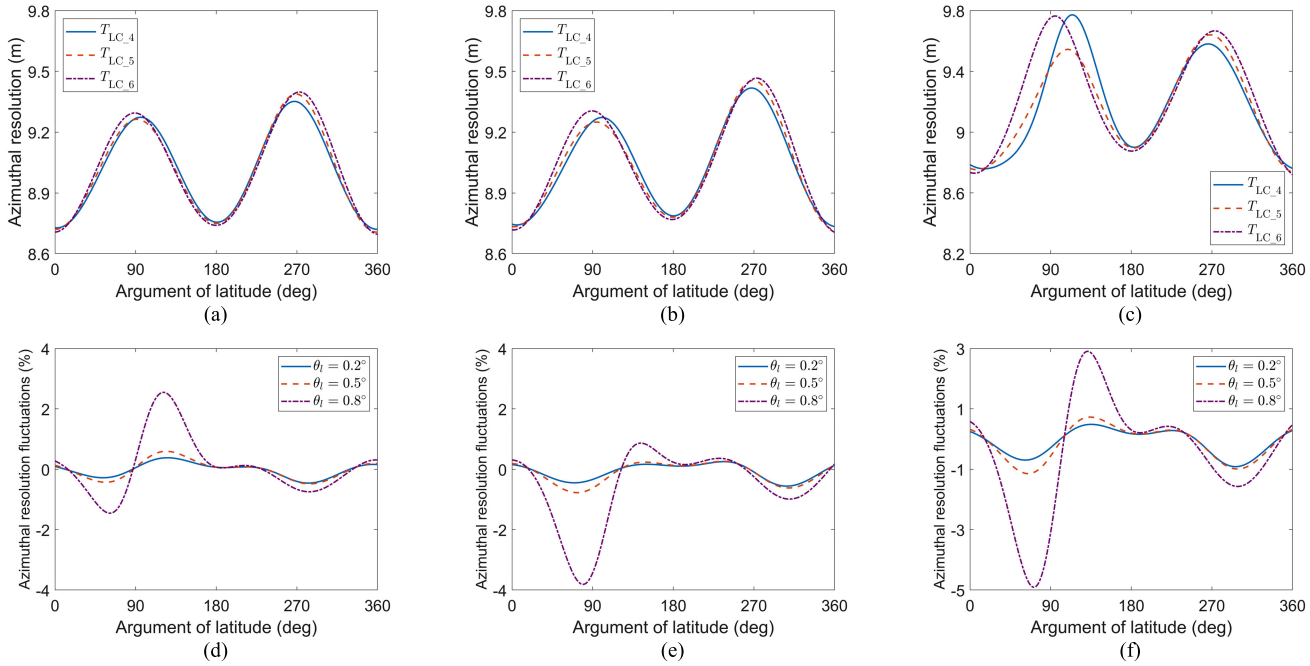

Fig. 9. In cycles T_{LC_4}∼T_{LC_6}, the azimuthal resolution versus the AOL of the LBSAR with look angles of (a) 0.2°, (b) 0.5°, and (c) 0.8°. The relative errors with various look angles versus the AOL, where (d) is Δ_{az_45}, (e) is Δ_{az_56}, and (f) is Δ_{az_46}.

perturbations could affect the distribution of LBSAR's azimuthal resolution along its orbit under a small orbital inclination condition.

Next, referring to cycles T_{LC_1}∼T_{LC_3}, we examine the variation of the azimuthal resolution against the AOL after a gap of 18.6 years, the period of orbital inclination variation. For this purpose, the azimuthal resolutions versus the AOL in cycles T_{LC_7}∼T_{LC_9} are illustrated in Fig. 10(a)–(c), while the relative errors of azimuthal resolution across different cycles are shown in Fig. 10(d)–(f).

Fig. 10 demonstrates that, after 18.6 years, the azimuthal resolution and its variation with respect to AOL are not exactly the same as that in Fig. 8 though it exhibits similar regularity. Thus, there is no specific cycle for the variation of azimuthal resolution under long-term orbital perturbations. The rationale for this aperiodic variation is that there are different periods associated with the LBSAR's orbital elements, and the azimuthal resolution suffers from coupling influences of those cyclically varying orbital elements. Notwithstanding, a clear trend can be observed: there is a notable peak

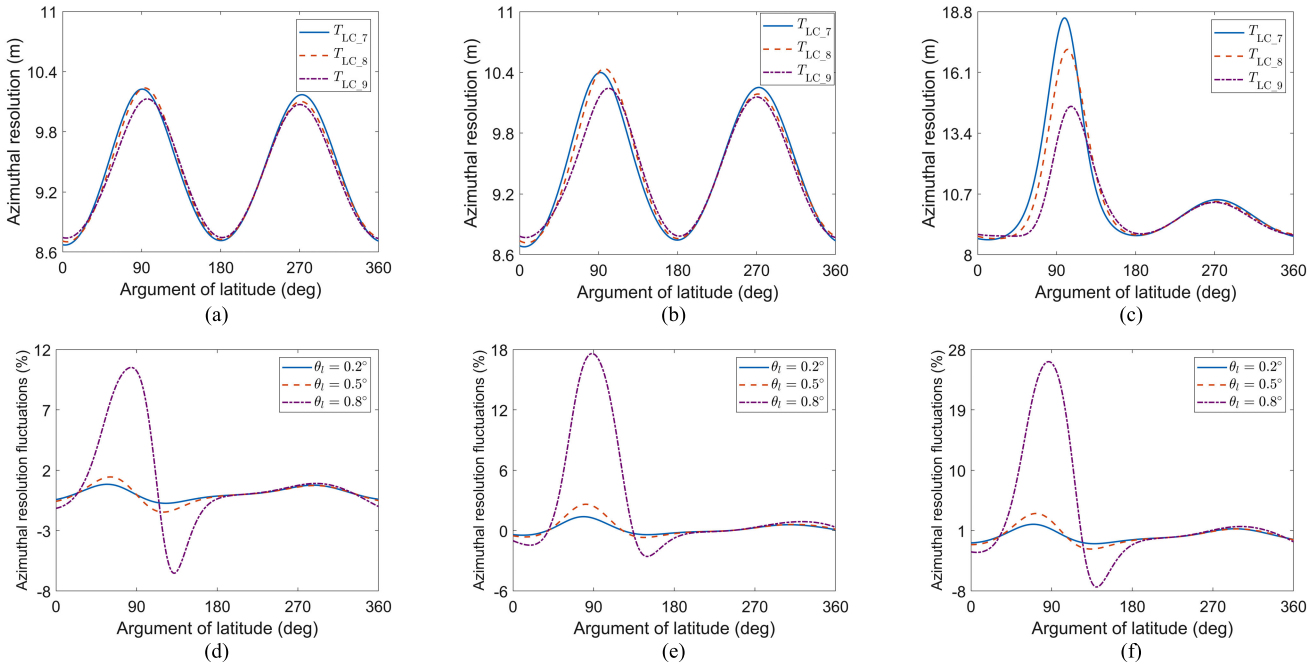

Fig. 10. In cycles T_{LC_7}∼T_{LC_9}, the azimuthal resolution versus the AOL of the LBSAR with look angles of (a) 0.2°, (b) 0.5°, and (c) 0.8°. The relative errors with various look angles versus the AOL, where (d) is Δ_{az_78}, (e) is Δ_{az_89}, and (f) is Δ_{az_79}.

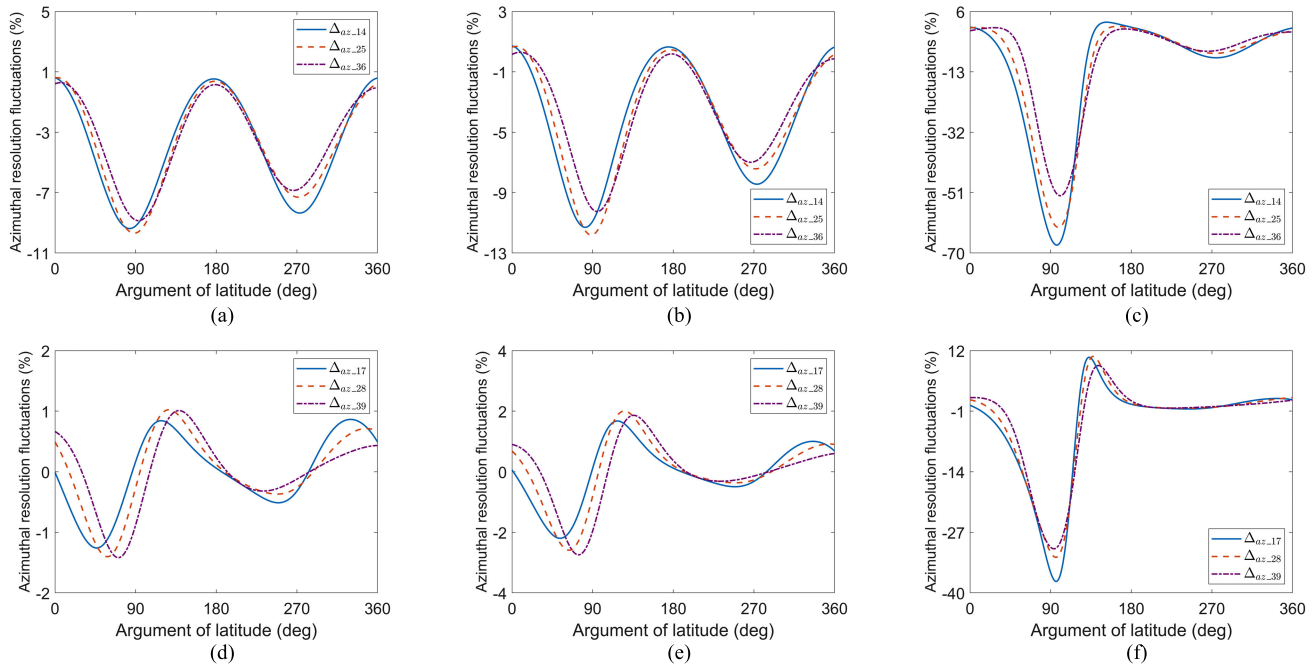

Fig. 11. Relative error of azimuthal resolution in cycles T_{LC_1}∼T_{LC_3} to that in cycles T_{LC_4}∼T_{LC_6} with the LBSAR look angles of (a) 0.2°, (b) 0.5°, and (c) 0.8°. The relative error of azimuthal resolution in cycles T_{LC_1}∼T_{LC_3} to that in cycles T_{LC_7}∼T_{LC_9} with the LBSAR look angles of (d) 0.2°, (e) 0.5°, and (f) 0.8°.

in the variation curve of azimuthal resolution for the LBSAR with a large look angle when the orbital inclination is large. The maximal fluctuation of azimuthal resolution between each cycle can approach 28% for a look angle of 0.8° in this event. Accordingly, the long-term orbital perturbation effects tend to affect the magnitude of azimuthal resolution under a large orbital inclination condition, and this phenomenon is most prominent in the case of a large look angle.

For a more rigorous analysis, we investigate the long-term orbital perturbation effects over long intervals by evaluating the fluctuations of azimuthal resolutions under various look angles. Thereupon, the relative errors of azimuthal resolutions in cycles T_{LC_1}∼T_{LC_3} to those in cycles T_{LC_4}∼T_{LC_6} are plotted in Fig. 11(a)–(c) as a function of the AOL. Furthermore, Fig. 11(d) and (e) displays the relative errors of azimuthal resolutions between cycles T_{LC_1}∼T_{LC_3} and T_{LC_7} ∼ T_{LC_9} against the AOL.

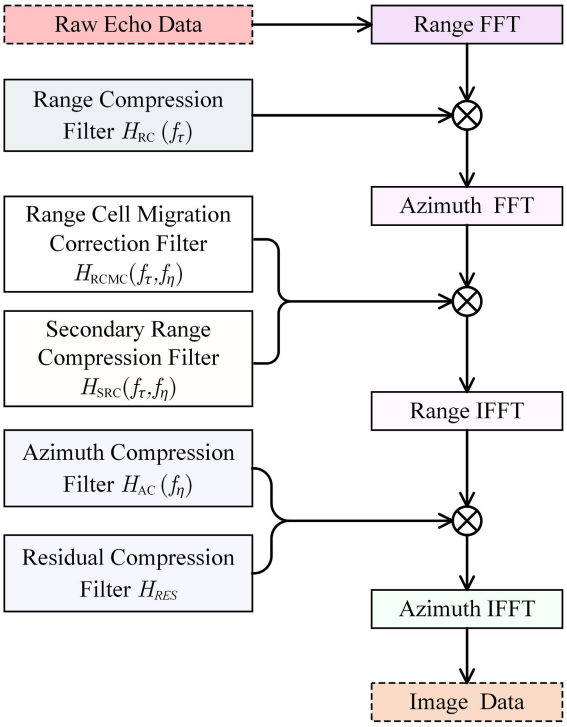

Fig. 12. Flowchart of signal processing for imaging formation in LBSAR.

As indicated in Fig. 11, the LBSAR azimuthal resolution varies obviously even at a small look angle after a period of 9.3 years. The maximal fluctuations in azimuthal resolution are around 10% for the look angles of 0.2° and 0.5°. As to the look angle of 0.8°, the fluctuations of azimuthal resolution can exceed 50%. When taking into account a period of orbital inclination variation, i.e., 18.6 years, the fluctuation of azimuthal resolution lessens in the LBSAR. However, Fig. 11(f) shows that the fluctuation magnitude of azimuthal resolution is still close to 40%, indicating the variation in azimuthal resolution remains significant after 18.6 years in the case of a large look angle. Moreover, the fluctuation of azimuthal resolution and its variation pattern respecting the AOL change considerably from cycle to cycle, confirming that the azimuthal resolution exhibits aperiodic behavior. Consequently, the long-term orbital perturbation effects deserve special care in the LBSAR.

IV. Simulations of the Point Target Responses

This section simulates the point target responses in the LBSAR to visualize the theoretical analysis presented in Section III. The key procedures of LBSAR signal processing are illustrated in Fig. 12. Specifically, the LBSAR signal is processed in the frequency domain by applying the range and azimuth fast Fourier transforms (FFTs). After the phase compensation and inverse FFT (IFFT), the echo data can be transformed into the 2-D time domain, allowing us to obtain the focused target response. The procedures and corresponding matched filters can be found in [21] and [23] with additional details. For simplicity, they are excluded from this study. Since this study primarily concerns the LBSAR's azimuthal resolution, only the azimuthal cuts of point target responses are presented in what follows.

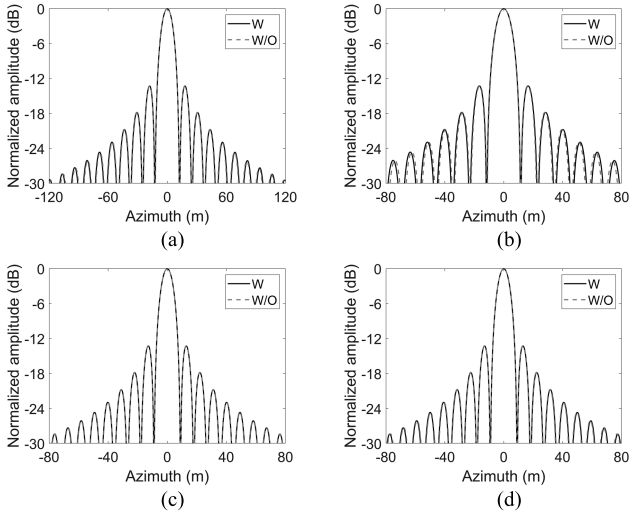

Fig. 13. Azimuthal profile in the LBSAR at the AOL of 60° in cycles: (a) T_{LC_1}, (b) T_{LC_2}, (c) T_{LC_4}, and (d) T_{LC_5}, where W/O represents the azimuthal profile without considering orbital perturbations and W represents the azimuthal profile with considering orbital perturbations.

TABLE III
Quality Measure of the Azimuthal Profile at the AOL of 60° With and Without Orbital Perturbations Within the SAT

	Parameters \ Cycles	T_{LC_1}	T_{LC_2}	T_{LC_4}	T_{LC_5}
W/O	Resolution (m)	12.41	11.38	8.95	9.07
	PSLR (dB)	-13.25	-13.24	-13.22	-13.24
	ISLR (dB)	-9.92	-9.91	-9.89	-9.90
W	Resolution (m)	12.53	11.55	8.95	9.08
	PSLR (dB)	-13.24	-13.25	-13.24	-13.24
	ISLR (dB)	-9.92	-9.90	-9.89	-9.89

To begin with, Fig. 13 presents azimuthal profiles with and without short-term orbital perturbations. In this case, four cycles, i.e., T_{LC_1}, T_{LC_2} and T_{LC_4}, T_{LC_5}, are considered. In each cycle, the LBSAR is located at $u_0 = 60°$ with a look angle of 0.8°. In this case, to demonstrate the impacts of short-term orbital perturbations on the azimuthal resolution, the point target responses of the LBSAR are simulated using the Doppler parameters with and without the short-term orbital perturbations. Table III summarizes numeric measures of the azimuthal resolution, peak-to-sidelobe ratio (PSLR), and integrated sidelobe ratio (ISLR).

As shown in Fig. 13 and Table III, the variation in azimuthal resolution caused by the short-term orbital perturbation is pretty small. Thus, the short-term orbital perturbation effect could affect LBSAR's azimuthal resolution, but to a small extent. The finding is also valid at other locations and in other cycles; for simplicity, a similar analysis is not repeated here. Notably, this study is conducted from a system configuration perspective; careful inspection is still necessary when it comes to exploiting the osculating orbit for signal processing in the LBSAR, as suggested in [27] and [29].

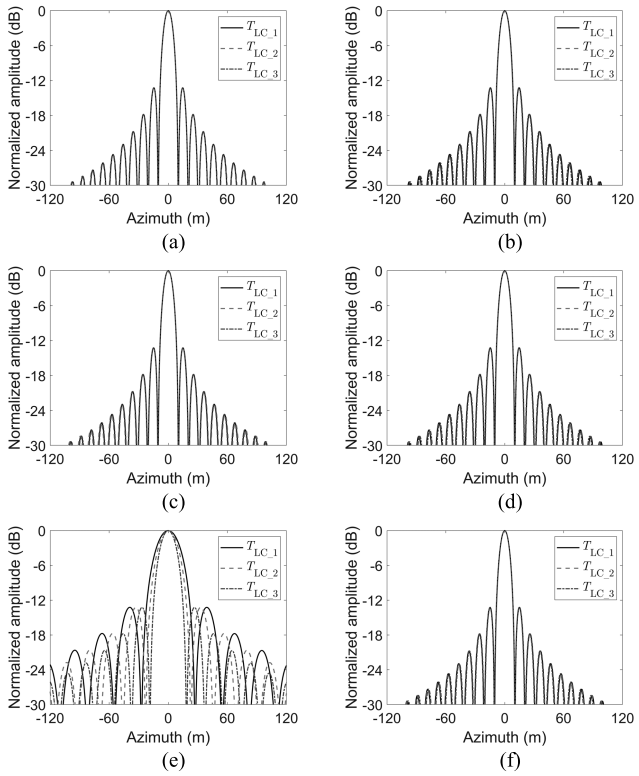

Fig. 14. In cycles T_{LC_1}~T_{LC_3}, the azimuthal profiles with a look angle of 0.2° at the AOL: (a) 90° and (b) 270°; the azimuthal profiles with a look angle of 0.5° at the AOL: (c) 90° and (d) 270°; and the azimuthal profiles with a look angle of 0.8° at the AOL: (e) 90° and (f) 270°.

TABLE IV
MEASURES OF SIMULATED RESOLUTION FOR THE AZIMUTHAL PROFILE AT AOLS OF 90° AND 270° IN CYCLES T_{LC_1}~T_{LC_3}

AOL	Cycle	$\theta_l = 0.2°$	$\theta_l = 0.5°$	$\theta_l = 0.8°$
90°	T_{LC_1}	10.22 m	10.39 m	27.27 m
	T_{LC_2}	10.26 m	10.49 m	22.93 m
	T_{LC_3}	10.21 m	10.37 m	18.62 m
270°	T_{LC_1}	10.21 m	10.29 m	10.48 m
	T_{LC_2}	10.14 m	10.21 m	10.38 m
	T_{LC_3}	10.10 m	10.18 m	10.34 m

The maximal relative error between the numeric resolution of simulated azimuthal profile and the theoretical one is 4.63×10^{-3}.

Next, the variations of azimuthal resolution in the LBSAR under long-term orbital perturbations are illustrated by the target responses. The azimuthal profiles with various look angles at the AOLs of 90° and 270° in cycles T_{LC_1}~T_{LC_3} are plotted in Fig. 14. The numeric simulated azimuthal resolutions are summarized in Table IV.

Inspections of Fig. 14 and Table IV reveal that the LBSAR's azimuthal resolution trends to be coarser with an increasing look angle. This variation is also dependent on the orbiting cycle and location of the LBSAR. For look angles of 0.2° and 0.5°, corresponding to middle and low latitudes, respectively, the azimuthal resolution is around 10 m in each cycle. As to a look angle of 0.8°, the azimuthal resolution at the AOL of 270° remains around 10 m with slight variations in each cycle. At the AOL of 90°, however, the LBSAR's azimuthal resolution becomes coarser and varies significantly across different cycles, ranging from 18.6 to 27.3 m. In this case, the azimuthal resolution is evidently influenced by long-term orbital perturbations.

TABLE V
NUMERIC MEASURES OF SIMULATED RESOLUTION FOR THE AZIMUTHAL PROFILE AT AOLS OF 90° AND 270° IN CYCLES T_{LC_4}~T_{LC_6}

AOL	Cycle	$\theta_l = 0.2°$	$\theta_l = 0.5°$	$\theta_l = 0.8°$
90°	T_{LC_4}	9.28 m	9.26 m	9.47 m
	T_{LC_5}	9.27 m	9.26 m	9.45 m
	T_{LC_6}	9.31 m	9.32 m	9.78 m
270°	T_{LC_4}	9.36 m	9.42 m	9.59 m
	T_{LC_5}	9.40 m	9.46 m	9.65 m
	T_{LC_6}	9.41 m	9.48 m	9.67 m

The maximal relative error between the numeric resolution of simulated azimuthal profile and the theoretical one is 2.41×10^{-3}.

TABLE VI
NUMERIC MEASURES OF SIMULATED RESOLUTION FOR THE AZIMUTHAL PROFILE AT AOLS OF 90° AND 270° IN CYCLES T_{LC_7}~T_{LC_9}

AOL	Cycle	$\theta_l = 0.2°$	$\theta_l = 0.5°$	$\theta_l = 0.8°$
90°	T_{LC_7}	10.24 m	10.41 m	17.55 m
	T_{LC_8}	10.24 m	10.42 m	15.75 m
	T_{LC_9}	10.12 m	10.17 m	12.98 m
270°	T_{LC_7}	10.18 m	10.25 m	10.45 m
	T_{LC_8}	10.10 m	10.19 m	10.38 m
	T_{LC_9}	10.07 m	10.17 m	10.34 m

The maximal relative error between the numeric resolution of simulated azimuthal profile and the theoretical one is 3.88×10^{-3}.

Using the same configurations shown in Fig. 14, we simulate the LBSAR's azimuthal profiles at AOLs of 90° and 270° in cycles T_{LC_4}~T_{LC_6} and T_{LC_7}~T_{LC_9}, and the results are presented in Figs. 15 and 16, respectively. Furthermore, the numeric measures of simulated azimuthal resolutions are also provided in Tables V and VI for comparison.

Comparing Fig. 15 and Table V with Fig. 14 and Table IV states that the azimuthal resolution is improved under the small orbital inclination condition when the LBSAR configurations remain the same. In this event, the variations of azimuthal resolution across different cycles lessen. As a result, it is expected that finer and more uniform azimuthal resolution is available by LBSAR when the orbital inclination is small. After a period of 18.6 years, the azimuthal resolution reverts to a coarser degree, as observed in Fig. 16 and Table VI. Moreover, for the LBSAR with a large look angle (e.g., 0.8°), the azimuthal resolution deteriorates once more at the AOL of 90°. Also, the variations of azimuthal resolution across different cycles become notable again. The comparison of Fig. 16 and Table VI with Fig. 14 and Table IV reveals

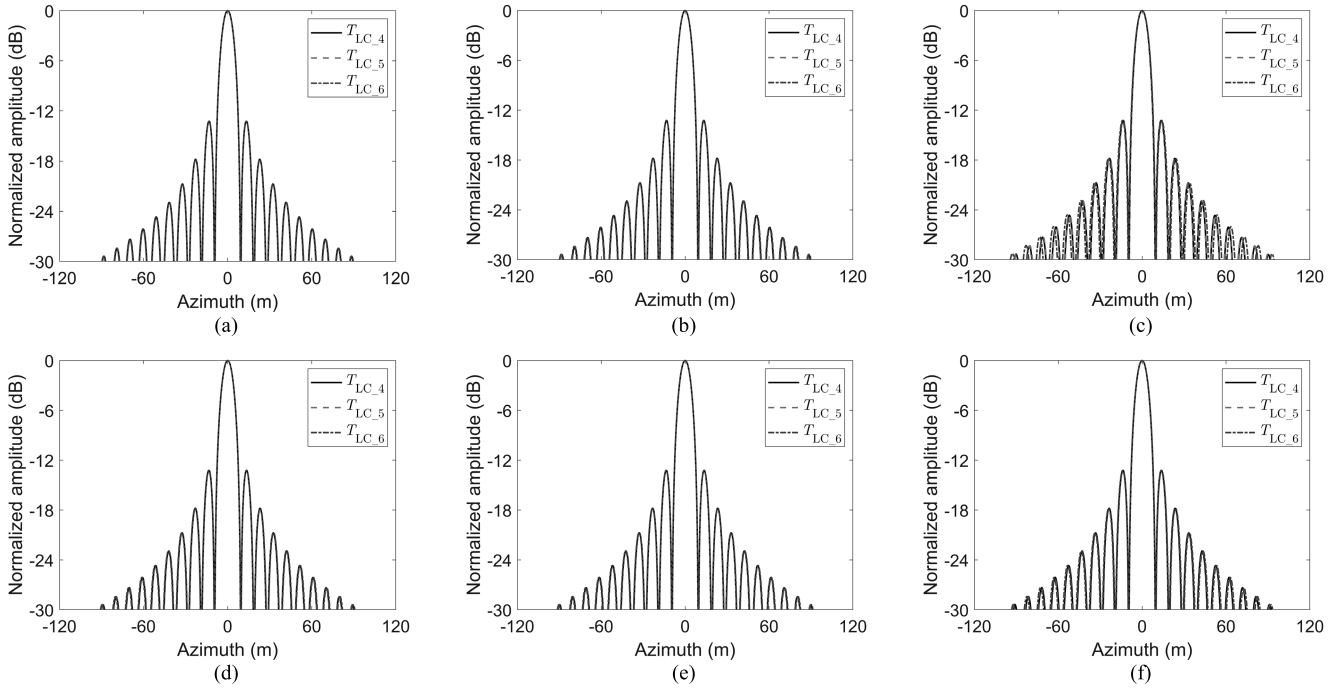

Fig. 15. In cycles T_{LC_4}∼T_{LC_6}, the azimuthal profiles at the AOL of 90° with look angles of (a) 0.2°, (b) 0.5°, and (c) 0.8°; the azimuthal profiles at the AOL of 270° with look angles of (d) 0.2°, (e) 0.5°, and (f) 0.8°.

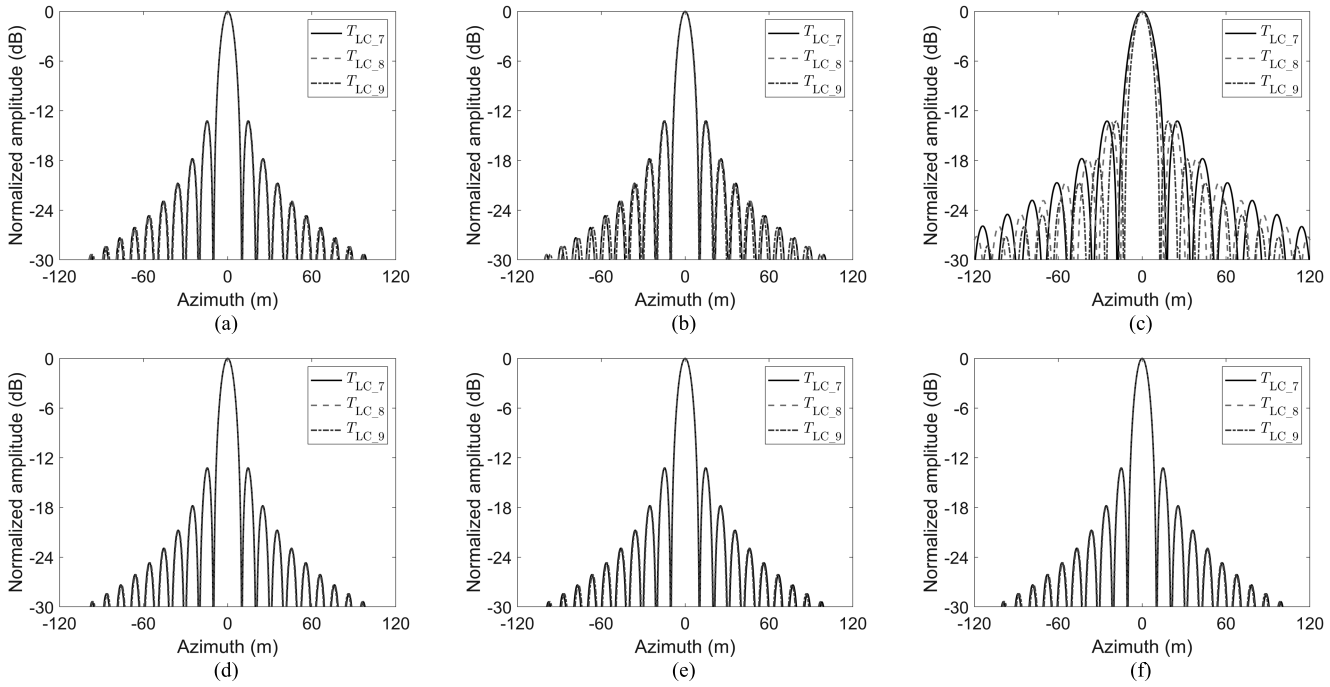

Fig. 16. In cycles T_{LC_7}∼T_{LC_9}, the azimuthal profiles at the AOL of 90° with look angles of (a) 0.2°, (b) 0.5°, and (c) 0.8°; the azimuthal profiles at the AOL of 270° with look angles of (d) 0.2°, (e) 0.5°, and (f) 0.8°.

the LBSAR's azimuthal resolution varies oscillatory. All simulation and analysis results suggest that the long-term orbital perturbation effects could noticeably influence Earth observations, which should be paid close attention to in the LBSAR.

V. Conclusion

This article investigates the orbital perturbation effects on the azimuthal resolution of the LBSAR in relation to orbital elements and SAR configurations. The findings show that the long-term orbital perturbation could significantly impact the LBSAR's azimuthal resolution, further leading to its aperiodic variations over different cycles. Such aperiodic variation patterns, most distinguished for a large look angle condition, are associated with the periodical varying orbital inclination. Specifically, the long-term orbital perturbations can give rise to fluctuations in azimuthal resolution between different cycles under the large orbital inclination condition, the maximal

magnitude of which can be up to over 30%. When the orbital inclination is small, the orbital perturbations tend to shift the peak location of the variation curve for azimuthal resolution in different cycles, with an overall fluctuation below 5%. Once the secular Earth observation by LBSAR is considered, there are higher fluctuations and irregular variations in the azimuthal resolution. Another issue regarding the perturbation effects is the short-term orbital perturbation, which could affect the azimuthal resolution to a small extent, with fluctuation below 3% in general.

In the future, the spatiotemporal analysis regarding the SAR's DFMR and azimuthal resolution can be conducted under the general framework proposed in this study. Since the LBSAR is essentially different from spaceborne SAR, many coupling orbital and radar parameters, and their net effects on its observation performance deserve a deeper look. One example is the swath width, which is of concern in observing super events (e.g., superhurricanes) on Earth. Future work shall involve such temporal-spatial analysis of swath width variation on the basis of this study.

APPENDIX

According to (4) and (5), there are four terms in the DFMR of the SAR system, namely,

$$\Re_1 = R_{\mathrm{ST}}^{-1} \cdot (\mathbf{V_{SAR}} \cdot \mathbf{V_{SAR}}) + \left(R_{\mathrm{ST}}^{-1} \cdot \mathbf{R_{ST}}\right) \cdot \mathbf{A_{SAR}} \tag{A1a}$$

$$\Re_2 = -2R_{\mathrm{ST}}^{-1} \cdot (\mathbf{V_{SAR}} \cdot \mathbf{V_{TOI}}) \tag{A1b}$$

$$\Re_3 = R_{\mathrm{ST}}^{-1} \cdot \mathbf{V_{TOI}} \cdot \mathbf{V_{TOI}} - R_{\mathrm{ST}}^{-1} \cdot \mathbf{A_{TOI}} \cdot \mathbf{R_{ST}} \tag{A1c}$$

$$\Re_4 = -R_{\mathrm{ST}}^{-3} \cdot [(\mathbf{V_{SAR}} - \mathbf{V_{TOI}}) \cdot \mathbf{R_{ST}}]^2. \tag{A1d}$$

Consider the first term in (A1a). For a Keplerian orbit, the SAR velocity vector in the ACS can be written as

$$\mathbf{V_{SAR}^{ACS}} = \mathbf{p} \cdot V_{\mathrm{kep}} \tag{A2}$$

with

$$\mathbf{p} = [(e\cos\nu + 1), 0, -e\sin\nu]^T \tag{A2a}$$

$$V_{\mathrm{kep}} = \sqrt{\mu \cdot a^{-1} \cdot \left(1 - e^2\right)^{-1}}. \tag{A2b}$$

A squared norm of the SAR velocity vector should be considered, yielding the following relationship:

$$R_{\mathrm{ST}}^{-1} \cdot (\mathbf{V_{SAR}} \cdot \mathbf{V_{SAR}}) = R_{\mathrm{ST}}^{-1} \cdot V_{\mathbf{kep}}^2 \left(1 + e^2 + 2e\cos v\right). \tag{A3}$$

As the SAR acceleration vector in the Keplerian orbit, it is determined by

$$\mathbf{A_{SAR}} = -\mu R_{\mathrm{SAR}}^{-3} \cdot \mathbf{R_{SAR}}. \tag{A4}$$

The inner product of $R_{\mathrm{ST}}^{-1} \cdot \mathbf{R_{ST}}$and $\mathbf{A_{SAR}}$ is then expressed by

$$\begin{aligned} R_{\mathrm{ST}}^{-1}\mathbf{R_{ST}} \cdot \mathbf{A_{SAR}} &= R_{\mathrm{ST}}^{-1}\mathbf{R_{ST}} \cdot \left(-\mu R_{\mathrm{SAR}}^{-3}\mathbf{R_{SAR}}\right) \\ &= -\mu R_{\mathrm{SAR}}^{-2} \cdot \mathbf{R_{SAR}}\mathbf{R_{ST}}/(R_{\mathrm{SAR}}R_{\mathrm{ST}}) \\ &= -\mu R_{\mathrm{SAR}}^{-2}\cos\theta_l. \end{aligned} \tag{A5}$$

Taking account of (A3) and (A5), one can write (A1a) as

$$\Re_1^{\mathrm{kep}} = -\mu \cdot R_{SAR}^{-2} \cdot \cos\theta_l + R_{ST}^{-1} \cdot V_{\mathrm{kep}}^2 \left(1 + e^2 + 2e\cos v\right). \tag{A6}$$

Regarding the perturbed orbit of the LBSAR, the DE 430 provides the Moon's velocity vector in the ECI. Thus, we have

$$R_{\mathrm{ST}}^{-1} \cdot (\mathbf{V_{SAR}} \cdot \mathbf{V_{SAR}}) = R_{\mathrm{ST}}^{-1} \cdot \left(\mathbf{V_{SAR}^{ECI}} \cdot \mathbf{V_{SAR}^{ECI}}\right). \tag{A7}$$

The second term in (A1a) requires the representation of the vector $\mathbf{R_{ST}}$. In the ACS, it is signified as

$$\mathbf{R_{ST}^{ACS}} = -[R_{\mathrm{ST}}\sin\theta_l\cos\phi, -R_{\mathrm{ST}}\sin\theta_l\sin\phi, R_{\mathrm{ST}}\cos\theta_l]^T \tag{A8}$$

with R_{ST} taking the form of

$$R_{\mathrm{ST}} = R_{\mathrm{SAR}}\cos\theta_l - \left(R_{\mathrm{TOI}}^2 - R_{\mathrm{SAR}}^2\sin^2\theta_l\right)^{0.5}. \tag{A9}$$

As a result, one can yield

$$R_{\mathrm{ST}}^{-1} \cdot \mathbf{R_{ST}} = [-\sin\theta_l\cos\phi, \sin\theta_l\sin\phi, -\cos\theta_l]^T. \tag{A10}$$

The LBSAR acceleration vector, expressed in the ACS, is

$$\mathbf{A_{SAR}^{ACS}} = \mathbf{M}_2^{-1}\mathbf{M}_1^{-1}\mathbf{A_{SAR}^{ECI}} \tag{A11}$$

with

$$\mathbf{M}_1 = \mathbf{R}_z(-\Omega)\mathbf{R}_x(-i)\mathbf{R}_z(-u) \tag{A12}$$

$$\mathbf{M_2} = \begin{bmatrix} 0 & 0 & -1 \\ 1 & 0 & 0 \\ 0 & -1 & 0 \end{bmatrix} \tag{A13}$$

$$\mathbf{R}_x(\theta) = \begin{bmatrix} 1 & 0 & 0 \\ 0 & \cos\theta & \sin\theta \\ 0 & -\sin\theta & \cos\theta \end{bmatrix} \tag{A14}$$

$$\mathbf{R}_z(\theta) = \begin{bmatrix} \cos\theta & \sin\theta & 0 \\ -\sin\theta & \cos\theta & 0 \\ 0 & 0 & 1 \end{bmatrix} \tag{A15}$$

where $\mathbf{A_{SAR}^{ECI}} = [A_x^{\mathrm{ECI}}, A_y^{\mathrm{ECI}}, A_z^{\mathrm{ECI}}]^T$ is the SAR acceleration in the ECI, which can be numerically obtained by the DE 430.

Through coordinate transformation, one can write three components of the vector $\mathbf{A_{SAR}^{ACS}}$ as

$$\begin{cases} A_x^{\mathrm{ACS}} = -A_x^{\mathrm{ECI}} \cdot (\sin u\cos\Omega + \cos i\cos u\sin\Omega) \\ \qquad + A_y^{\mathrm{ECI}} \cdot (\cos i\cos u\cos\Omega - \sin u\sin\Omega) \\ \qquad + A_z^{\mathrm{ECI}} \cdot \sin i\cos u \\ A_y^{\mathrm{ACS}} = -A_x^{\mathrm{ECI}} \cdot \sin i\sin\Omega + A_y^{\mathrm{ECI}} \cdot \sin i\cos\Omega - A_z^{\mathrm{ECI}} \cdot \cos i \\ A_z^{\mathrm{ACS}} = -A_x^{\mathrm{ECI}} \cdot (\cos u\cos\Omega - \cos i\sin u\sin\Omega) \\ \qquad - A_y^{\mathrm{ECI}} \cdot (\cos u\sin\Omega + \cos i\sin u\cos\Omega) \\ \qquad - A_z^{\mathrm{ECI}} \cdot \sin i\sin u. \end{cases} \tag{A16}$$

Afterward, the second term in (A1a) can be expressed in terms of (A10) and (A16)

$$\begin{aligned} R_{\mathrm{ST}}^{-1}\mathbf{R_{ST}}\mathbf{A_{SAR}} = A_Y^{\mathrm{ACS}}\sin\theta_l\sin\phi - A_X^{\mathrm{ACS}}\sin\theta_l \\ \times \cos\phi - A_Z^{\mathrm{ACS}}\cos\theta_l. \end{aligned} \tag{A17}$$

As a result, one arrives at the expression of the term $\Re_1$ in the perturbed orbit

$$\begin{aligned} \Re_1^{\mathrm{per}} = R_{\mathrm{ST}}^{-1} \cdot \left(\mathbf{V_{SAR}^{ECI}} \cdot \mathbf{V_{SAR}^{ECI}}\right) \\ - A_x^{\mathrm{ACS}}\sin\theta_l\cos\phi + A_y^{\mathrm{ACS}}\sin\theta_l\sin\phi - A_z^{\mathrm{ACS}}\cos\theta_l. \end{aligned} \tag{A18}$$

Now, we focus attention on deriving (A1b). The linear velocity vector of TOI caused by Earth's rotation is defined as

$$\mathbf{V_{TOI}} = w_E \times \mathbf{R_{TOI}} = \omega_E \cdot \mathbf{k} \times \mathbf{R_{TOI}} \tag{A19}$$

where $\mathbf{k} = [0, 0, 1]^T$ and ω_E is the angular velocity of Earth's rotation. From (A19), one can get

$$\mathbf{V_{SAR}} \cdot \mathbf{V_{TOI}} = \omega_E \cdot [\mathbf{V_{SAR}} \cdot (\mathbf{k} \times \mathbf{R_{TOI}})]. \tag{A20}$$

In the ACS, the vector $\mathbf{k}$ is represented as

$$\mathbf{k^{ACS}} = \mathbf{M_2^{-1}} \mathbf{M_1^{-1}} \cdot \mathbf{k}. \tag{A21}$$

Equation (A21) can be equivalently written by

$$\mathbf{k}^{\mathrm{ACS}} = [\sin i \cos u, -\cos i, -\sin i \sin u]^T. \tag{A22}$$

As for the TOI's position vector, in the ACS, it takes the following form:

$$\mathbf{R_{TOI}^{ACS}} = [R_{\mathrm{ST}} \sin\theta_l \cos\phi, -R_{\mathrm{ST}} \sin\theta_l \sin\phi, R_{\mathrm{ST}} \cos\theta_l - R_{\mathrm{SAR}}]^T. \tag{A23}$$

Then, the cross-product $\mathbf{k} \times \mathbf{R_{TOI}}$ takes the expression of

$$\begin{aligned}\mathbf{k} \times \mathbf{R_{TOI}} &= \mathbf{k}^{\mathrm{ACS}} \times \mathbf{R}_{\mathrm{TOI}}^{\mathrm{ACS}} \\ &= \begin{bmatrix} \cos i (R_{\mathrm{SAR}} - R_{\mathrm{ST}} \cos\theta_l) - R_{\mathrm{ST}} \sin i \sin u \sin\theta_l \sin\phi \\ \sin i \cos u (R_{\mathrm{SAR}} - R_{\mathrm{ST}} \cos\theta_l) - R_{\mathrm{ST}} \sin i \sin u \sin\theta_l \cos\phi \\ -\sin i \cos u (R_{\mathrm{ST}} \sin\theta_l \sin\phi) + R_{\mathrm{ST}} \sin\theta_l \cos\phi \cos i \end{bmatrix}.\end{aligned} \tag{A24}$$

The expression of the above equation remains the same regardless of the orbital shape. However, the SAR motion is sensitive to orbital perturbations. The expression of the SAR velocity vector in the Keplerian orbit is already given in (A2). Regarding the SAR velocity vector in the perturbed orbit, it has the form of

$$\mathbf{V_{SAR}^{ACS}} = \mathbf{M_2^{-1}} \mathbf{M_1^{-1}} \mathbf{V_{SAR}^{ECI}}. \tag{A25}$$

By the same argument in (A11), (A25) can be equivalently written as

$$\begin{cases} V_x^{\mathrm{ACS}} = -V_x^{\mathrm{ECI}} \cdot (\sin u \cos\Omega + \cos i \cos u \sin\Omega) \\ \qquad\quad + V_y^{\mathrm{ECI}} \cdot (\cos i \cos u \cos\Omega - \sin u \sin\Omega) \\ \qquad\quad + V_z^{\mathrm{ECI}} \cdot \sin i \cos u \\ V_y^{\mathrm{ACS}} = 0 \\ V_z^{\mathrm{ACS}} = -V_x^{\mathrm{ECI}} \cdot (\cos u \cos\Omega - \cos i \sin u \sin\Omega) \\ \qquad\quad - V_y^{\mathrm{ECI}} \cdot (\cos u \sin\Omega + \cos i \sin u \cos\Omega) \\ \qquad\quad - V_z^{\mathrm{ECI}} \cdot \sin i \sin u \end{cases} \tag{A26}$$

where $\mathbf{V_{SAR}^{ECI}} = [V_x^{\mathrm{ECI}}, V_y^{\mathrm{ECI}}, V_z^{\mathrm{ECI}}]^T$ is the velocity vector of the SAR system in the ECI.

In the Keplerian orbit, from (A1b), (A2), (A20), and (A24), the term $\Re_2$ can be explicitly expressed by

$$\begin{aligned}\Re_2^{\mathrm{kep}} = & -2R_{\mathrm{ST}}^{-1} \cdot \omega_E \cdot V_{\mathrm{kep}} \\ & \cdot \{(e\cos\nu + 1) \cdot [(R_{\mathrm{SAR}} - R_{\mathrm{ST}} \cos\theta_l) \cos i \\ & \qquad - R_{\mathrm{ST}} \sin\theta_l \sin\phi \sin i \sin u] \\ & + e \cdot R_{\mathrm{ST}} \sin\theta_l \sin\nu \\ & \cdot (-\cos\phi \cos i + \sin\phi \sin i \cos u)\}.\end{aligned} \tag{A27}$$

In the perturbed orbit, the term $\Re_2$ can be obtained in line with (A1b), (A20), (A24), and (A26), namely,

$$\begin{aligned}\Re_2^{\mathrm{per}} = & -2R_{ST}^{-1} \cdot \omega_E \\ & \cdot \left\{V_x^{\mathrm{ACS}} \cdot [(R_{\mathrm{SAR}} - R_{\mathrm{ST}} \cos\theta_l) \cos i \right. \\ & \qquad \left. - R_{\mathrm{ST}} \sin\theta_l \sin\phi \sin i \sin u] \right. \\ & \left. - V_z^{\mathrm{ACS}} (R_{\mathrm{ST}} \sin\theta_l \cos\phi \cos i \right. \\ & \left. - R_{\mathrm{ST}} \sin\theta_l \sin\phi \sin i \cos u)\right\}.\end{aligned} \tag{A28}$$

Next, the representation of the term $\Re_3$ is exploited. According to (A19), we have the following relation:

$$V_{\mathrm{TOI}}^2 = \mathbf{V_{TOI}} \cdot \mathbf{V_{TOI}} = \omega_E^2 \cdot (\mathbf{k} \times \mathbf{R_{TOI}}) \cdot (\mathbf{k} \times \mathbf{R_{TOI}}). \tag{A29}$$

Substituting (A24) into (A29), we can simply write

$$\begin{aligned}V_{\mathrm{TOI}}^2 = & -2R_{\mathrm{ST}} R_{\mathrm{SAR}} \cos\theta_l \sin^2 i \cos^2 u \\ & + 2R_{\mathrm{ST}}^2 \cos\theta_l \sin\theta_l \sin\phi \cos i \sin i \sin u \\ & - 2R_{\mathrm{ST}}^2 \sin^2\theta_l \cos\phi \sin\phi \cos i \sin i \cos u \\ & + 2R_{\mathrm{ST}}^2 \cos\theta_l \sin\theta_l \cos\phi \sin^2 i \cos u \sin u \\ & - 2R_{\mathrm{ST}} R_{\mathrm{SAR}} \sin\theta_l \cos\phi \sin^2 i \cos u \sin u \\ & - 2R_{\mathrm{ST}} R_{\mathrm{SAR}} \sin\theta_l \sin\phi \cos i \sin i \sin u \\ & + R_{\mathrm{SAR}}^2 \cos^2 i + R_{\mathrm{ST}}^2 \cos^2\theta_l \cos^2 i + R_{\mathrm{SAR}}^2 \sin^2 i \cos^2 u \\ & - 2R_{\mathrm{ST}} R_{\mathrm{SAR}} \cos\theta_l \cos^2 i + R_{\mathrm{ST}}^2 \sin^2\theta_l \cos^2 i \cos^2\phi \\ & + R_{\mathrm{ST}}^2 \cos^2\theta_l \sin^2 i \cos^2 u + R_{\mathrm{ST}}^2 \sin^2\theta_l \\ & \times \cos^2\phi \sin^2 i \sin^2 u \\ & + R_{\mathrm{ST}}^2 \sin^2\theta_l \sin^2\phi \sin^2 i \cos^2 u \\ & + R_{\mathrm{ST}}^2 \sin^2\theta_l \sin^2\phi \sin^2 i \sin^2 u.\end{aligned} \tag{A30}$$

Collecting and combining similar terms, (A30) can be simplified to

$$\begin{aligned}V_{\mathrm{TOI}}^2 = \omega_E^2 \cdot & \{(R_{\mathrm{SAR}} - R_{\mathrm{ST}} \cos\theta_l)^2 \cdot (1 - \sin^2 i \sin^2 u) \\ & + R_{\mathrm{ST}}^2 \sin^2\theta_l \\ & \cdot (1 - \sin^2\phi \cos^2 i - \cos^2\phi \sin^2 i \cos^2 u) \\ & - 2R_{\mathrm{ST}} \sin\theta_l \sin i \\ & \cdot [R_{\mathrm{ST}} \sin\theta_l \cos\phi \sin\phi \cos i \\ & \quad \times \cos u + \sin u \cdot (R_{\mathrm{SAR}} - R_{\mathrm{ST}} \cos\theta_l) \\ & \quad \times (\cos\phi \cos u \sin i + \sin\phi \cos i)]\}.\end{aligned} \tag{A31}$$

The second term in (A1c) requires providing the expression for the TOI acceleration vector given rise by Earth's rotation. By definition, it is signified as

$$\begin{aligned}\mathbf{A_{TOI}} &= w_E \times \mathbf{V_{TOI}} \\ &= w_E \times (w_E \times \mathbf{R_{TOI}}) \\ &= (w_E \cdot \mathbf{R_{TOI}}) \cdot w_E - \mathbf{R_{TOI}} \cdot (w_E \cdot w_E).\end{aligned} \tag{A32}$$

As a result, the inner product of $\mathbf{A_{TOI}}$and $\mathbf{R_{ST}}$ becomes

$$\begin{aligned}\mathbf{A_{TOI}} \cdot \mathbf{R_{ST}} &= [(w_E \cdot \mathbf{R_{TOI}}) \cdot w_E - \mathbf{R_{TOI}} \cdot (w_E \cdot w_E)] \cdot \mathbf{R_{ST}} \\ &= (\omega_E \mathbf{k} \cdot \mathbf{R_{TOI}}) \cdot \omega_E \mathbf{k} \cdot \mathbf{R_{ST}} - \omega_E^2 \cdot \mathbf{R_{TOI}} \cdot \mathbf{R_{ST}} \\ &= \omega_E^2 \cdot [(\mathbf{k} \cdot \mathbf{R_{TOI}}) \cdot (\mathbf{k} \cdot \mathbf{R_{ST}}) - \mathbf{R_{TOI}} \cdot \mathbf{R_{ST}}].\end{aligned} \tag{A33}$$

For simplify, the following notation is introduced:

$$\mathbf{A_{TOI}} \cdot \mathbf{R_{ST}} = \omega_E^2 \cdot (R_{\mathrm{A1}} - R_{\mathrm{A2}}) \tag{A34}$$

with

$$R_{\mathrm{A1}} = (\mathbf{k}\cdot\mathbf{R_{TOI}})\cdot(\mathbf{k}\cdot\mathbf{R_{ST}})) \tag{A35}$$
$$R_{\mathrm{A2}} = \mathbf{R_{TOI}}\cdot\mathbf{R_{ST}}. \tag{A36}$$

According to (A8), (A22), and (A23), the term R_{A1} can be written by

$$\begin{aligned} R_{\mathrm{A1}} = {} & 2R_{\mathrm{ST}}^2\cos i\cos\theta_l\sin i\sin\phi\sin\theta_l\sin u \\ & - 2R_{\mathrm{ST}}^2\cos i\cos\phi\cos u\sin i\sin\phi\sin^2\theta_l \\ & + 2R_{\mathrm{ST}}^2\cos\phi\cos\theta_l\cos u\sin^2 i\sin\theta_l\sin u \\ & - R_{\mathrm{ST}}R_{\mathrm{SAR}}\cos i\sin i\sin\phi\sin\theta_l\sin u \\ & - R_{\mathrm{ST}}R_{\mathrm{SAR}}\cos\phi\cos u\sin^2 i\sin\theta_l\sin u \\ & + R_{\mathrm{ST}}R_{\mathrm{SAR}}\cos\theta_l\sin^2 i\sin^2 u - R_{\mathrm{ST}}^2\cos^2\theta_l\sin^2 i\sin^2 u \\ & - R_{\mathrm{ST}}^2\cos^2 i\sin^2\phi\sin^2\theta_l \\ & - R_{\mathrm{ST}}^2\cos^2\phi\cos^2 u\sin^2 i\sin^2\theta_l. \end{aligned} \tag{A37}$$

Equation (A37) can be further simplified by combining similar terms, after which it is of the form

$$\begin{aligned} R_{\mathrm{A1}} = {} & R_{\mathrm{ST}}\cos\theta_l\sin^2 i\sin^2 u\cdot(R_{\mathrm{SAR}} - R_{\mathrm{ST}}\cos\theta_l) \\ & - R_{\mathrm{ST}}^2\sin^2\theta_l\cdot\left(\cos^2 i\sin^2\phi + \cos^2\phi\cos^2 u\sin^2 i\right) \\ & - R_{\mathrm{ST}}\sin\theta_l\sin i\sin u\cdot(R_{\mathrm{SAR}}\cos i\sin\phi \\ & + R_{\mathrm{SAR}}\cos\phi\cos u\sin i - 2R_{\mathrm{ST}}\cos\theta_l\sin\phi\cos i) \\ & + 2R_{\mathrm{ST}}^2\sin\theta_l\cos\phi\sin i\cos u \\ & \cdot(\cos\theta_l\sin i\sin u - \sin\theta_l\sin\phi\cos i). \end{aligned} \tag{A38}$$

Regarding (A36), it can be equivalently represented as

$$R_{\mathrm{A2}} = \mathbf{R_{TOI}}\cdot\mathbf{R_{SAR}} - \mathbf{R_{TOI}}\cdot\mathbf{R_{TOI}}. \tag{A39}$$

The first term in (A39), which is correlated with the geocentric angle between the TOI and SAR, is signified as

$$\begin{aligned} \mathbf{R_{TOI}R_{SAR}} &= R_{\mathrm{TOI}}R_{\mathrm{SAR}}\cdot\left(R_{\mathrm{TOI}}^{-1}\mathbf{R_{TOI}}\cdot R_{\mathrm{SAR}}^{-1}\mathbf{R_{SAR}}\right) \\ &= R_{\mathrm{TOI}}R_{\mathrm{SAR}}\cdot\cos\beta. \end{aligned} \tag{A40}$$

The law of cosines gives

$$R_{\mathrm{ST}}^2 = R_{\mathrm{SAR}}^2 + R_{\mathrm{TOI}}^2 - 2R_{\mathrm{SAR}}R_{\mathrm{TOI}}\cos\beta \tag{A41}$$
$$R_{\mathrm{TOI}}^2 = R_{\mathrm{SAR}}^2 + R_{\mathrm{ST}}^2 - 2R_{\mathrm{SAR}}R_{\mathrm{ST}}\cos\theta_l. \tag{A42}$$

Equation (A41) can be equivalently expressed as

$$\cos\beta = 0.5R_{\mathrm{SAR}}^{-1}R_{\mathrm{TOI}}^{-1}\cdot\left(R_{\mathrm{SAR}}^2 + R_{\mathrm{TOI}}^2 - R_{\mathrm{ST}}^2\right). \tag{A43}$$

In line with (A40) and (A43), (A39) can be written by

$$R_{\mathrm{A2}} = 0.5\cdot\left(R_{\mathrm{SAR}}^2 - R_{\mathrm{ST}}^2 - R_{\mathrm{TOI}}^2\right). \tag{A44}$$

Substituting (A42) into (A44), one yields

$$R_{\mathrm{A2}} = R_{\mathrm{SAR}}R_{\mathrm{ST}}\cos\theta_l - R_{\mathrm{ST}}^2. \tag{A45}$$

According to (A1c), (A29), and (A34), we have

$$\Re_3 = R_{\mathrm{ST}}^{-1}\cdot\left(V_{\mathrm{TOI}}^2 - \omega_E^2\cdot R_{\mathrm{A1}} + \omega_E^2\cdot R_{\mathrm{A2}}\right). \tag{A46}$$

Using (A31), (A33), (A38), and (A45), (A46) can be explicitly expressed as

$$\begin{aligned} \Re_3 = {} & \omega_E^2R_{\mathrm{ST}}^{-1}\cdot\{(R_{\mathrm{SAR}} - R_{\mathrm{ST}}\cos\theta_l)^2\cdot\left(1-\sin^2 i\sin^2 u\right) \\ & + R_{\mathrm{ST}}^2\sin^2\theta_l \\ & \cdot\left(1-\sin^2\phi\cos^2 i - \cos^2\phi\sin^2 i\cos^2 u\right) \\ & - 2R_{\mathrm{ST}}\sin\theta_l\sin i \\ & \cdot[R_{\mathrm{ST}}\sin\theta_l\cos\phi\sin\phi\cdot\cos i\cos u \\ & + \sin u\cdot(R_{\mathrm{SAR}} - R_{\mathrm{ST}}\cos\theta_l) \\ & \cdot(\cos\phi\cos u\sin i + \sin\phi\cos i)]\} \\ & - \omega_E^2R_{\mathrm{ST}}^{-1} \\ & \cdot\big[R_{\mathrm{ST}}\cos\theta_l\sin^2 i\sin^2 u\cdot(R_{\mathrm{SAR}} - R_{\mathrm{ST}}\cos\theta_l) \\ & - R_{\mathrm{ST}}^2\sin^2\theta_l \\ & \cdot\left(\cos^2 i\sin^2\phi + \cos^2\phi\cos^2 u\sin^2 i\right) \\ & - R_{\mathrm{ST}}\sin\theta_l\sin i\sin u\cdot(R_{\mathrm{SAR}}\cos i\sin\phi \\ & + R_{\mathrm{SAR}}\cos\phi\cos u\sin i \\ & - 2R_{\mathrm{ST}}\cos\theta_l\sin\phi\cos i) \\ & + 2R_{\mathrm{ST}}^2\sin\theta_l\cos\phi\sin i\cos u \\ & \cdot(\cos\theta_l\sin i\sin u - \sin\theta_l\sin\phi\cos i)\big] \\ & + \omega_E^2\cdot(R_{\mathrm{SAR}}\cos\theta_l - R_{\mathrm{ST}}). \end{aligned} \tag{A47}$$

There are plenty of similar terms in (A47); after simplification, we, finally, arrive at

$$\begin{aligned} \Re_3 = {} & R_{\mathrm{ST}}^{-1}\omega_E^2\cdot\{R_{\mathrm{SAR}}^2 - R_{\mathrm{SAR}}R_{\mathrm{ST}}\cos\theta_l \\ & + R_{\mathrm{SAR}}\sin^2 i\sin^2 u(R_{\mathrm{ST}}\cos\theta_l - R_{\mathrm{SAR}}) \\ & - R_{\mathrm{SAR}}R_{\mathrm{ST}}\sin\theta_l\sin i\sin u \\ & \cdot(\cos\phi\sin i\cos u + \sin\phi\cos i)\}. \end{aligned} \tag{A48}$$

The term $\Re_3$ relates to Earth's rotation only; thus, its expression remains the same with and without orbital perturbations.

Next, the derivation of the term $\Re_4$ is in order. This term can be further decomposed by considering the contribution of each component, as

$$\Re_{4\mathrm{E}} = -R_{\mathrm{ST}}^3\cdot(\mathbf{V_{TOI}}\cdot\mathbf{R_{ST}})^2 \tag{A49}$$
$$\Re_{4\mathrm{S}} = -R_{\mathrm{ST}}^{-3}\cdot(\mathbf{V_{SAR}}\cdot\mathbf{R_{ST}})^2 \tag{A50}$$
$$\Re_{4\mathrm{SE}} = 2R_{\mathrm{ST}}^{-3}\cdot[(\mathbf{V_{SAR}}\cdot\mathbf{R_{ST}})\cdot(\mathbf{V_{TOI}}\cdot\mathbf{R_{ST}})]. \tag{A51}$$

Equations (A49)–(A51) correlate to two inner products, namely, $\mathbf{V_{TOI}}\cdot\mathbf{R_{ST}}$ that has no dependency on the orbital perturbations and $\mathbf{V_{SAR}}\cdot\mathbf{R_{ST}}$ that is susceptible to the perturbation effects. From (A8) and (A19), the former inner product can be expressed as

$$\begin{aligned} \mathbf{V_{TOI}}\cdot\mathbf{R_{ST}} = {} & -\omega_E R_{\mathrm{SAR}}R_{\mathrm{ST}}\cdot\sin\theta_l \\ & \cdot(\sin\phi\sin i\cos u - \cos\phi\cos i). \end{aligned} \tag{A52}$$

As for the latter one, its expression in the Keplerian orbit could be obtained by considering (A2) and (A8)

$$\mathbf{V_{SAR}^{kep}R_{ST}} = R_{\mathrm{ST}}V_{\mathrm{kep}}\cdot[(e\cos\nu+1)\sin\theta_l\cos\phi - e\sin\nu\cos\theta_l]. \tag{A53}$$

In the perturbed orbit case, the inner product $\mathbf{V_{SAR}}\cdot\mathbf{R_{ST}}$ is determined by (A8) and (A26), which takes the form of

$$\mathbf{V_{SAR}^{per}R_{ST}} = R_{\mathrm{ST}}\cdot\left(V_x^{\mathrm{ACS}}\cdot\sin\theta_l\cos\phi + V_z^{\mathrm{ACS}}\cdot\cos\theta_l\right). \tag{A54}$$

Now, consider the term $\Re_{4\mathrm{E}}$. According to (A52), it has a fixed representation in spite of its orbital shape and is given by

$$\begin{aligned} \Re_{4\mathrm{E}} = {} & -\omega_E^2R_{\mathrm{SAR}}^2R_{\mathrm{ST}}^{-1}\sin^2\theta_l\cdot(\sin^2\phi\sin^2 i\cos^2 u \\ & + \cos^2\phi\cos^2 i - 2\sin\phi\cos\phi\cdot\sin i\cos i\cos u). \end{aligned} \tag{A55}$$

$$\mathbf{V}_{\mathbf{TOI}}^{\mathbf{ACS}} = \omega_E \begin{bmatrix} (R_{\mathrm{SAR}} - R_{\mathrm{ST}}\cos\theta_l)\cos i - R_{\mathrm{ST}}\sin\theta_l\sin\phi\sin i\sin u \\ (R_{\mathrm{SAR}} - R_{\mathrm{ST}}\cos\theta_l)\sin i\cos u - R_{\mathrm{ST}}\sin\theta_l\cos\phi\sin i\sin u \\ -R_{\mathrm{ST}}\sin\theta_l\sin\phi\sin i\cos u + R_{\mathrm{ST}}\sin\theta_l\cos\phi\cos i \end{bmatrix}. \tag{A63}$$

As for terms $\Re_{4\mathrm{S}}$ and $\Re_{4\mathrm{SE}}$, they are connected with the SAR motion. For the Keplerian orbit, both terms should take account of (A53), and they are expressed as

$$\begin{aligned}\Re_{4\mathrm{S}}^{\mathrm{kep}} = & -R_{\mathrm{ST}}^{-1}\cdot V_{\mathrm{kep}}^2 \\ & \cdot\left[(1+e\cos\nu)^2\cos^2\theta_l + e^2\sin^2\nu\sin^2\theta_l\cos^2\phi\right. \\ & \left. +2e\cdot\sin\nu\cdot(e\cos\nu+1)\cdot\sin\theta_l\cos\theta_l\cos\phi\right]\end{aligned} \tag{A56}$$

$$\begin{aligned}\Re_{4\mathrm{SE}}^{\mathrm{kep}} = & -2\omega_E R_{\mathrm{SAR}} R_{\mathrm{ST}}^{-1}\cdot V_{\mathrm{kep}}\cdot\sin\theta_l \\ & \cdot(\sin\phi\sin i\cos u - \cos\phi\cos i) \\ & \cdot[(e\cos\nu+1)\cdot\sin\theta_l\cos\phi + e\sin\nu\cos\theta_l].\end{aligned} \tag{A57}$$

In the case of perturbation effects, by virtue of (A54), $\Re_{4\mathrm{S}}$ and $\Re_{4\mathrm{SE}}$ are, respectively, represented by

$$\begin{aligned}\Re_{4\mathrm{S}}^{\mathrm{per}} = & -R_{\mathrm{ST}}^{-1}\cdot\left[\left(V_x^{\mathrm{ACS}}\right)^2\sin^2\theta_l\cos^2\phi\right. \\ & +\left(V_z^{\mathrm{ACS}}\right)^2\cos^2\theta_l \\ & \left.+2V_x^{\mathrm{ACS}}\cdot V_z^{\mathrm{ACS}}\sin\theta_l\cos\theta_l\cos\phi\right]\end{aligned} \tag{A58}$$

$$\begin{aligned}\Re_{4\mathrm{SE}}^{\mathrm{per}} = & -2\omega_E R_{\mathrm{SAR}} R_{\mathrm{ST}}^{-1}\cdot\sin\theta_l\cdot(\sin\phi\sin i\cos u \\ & -\cos\phi\cos i)\cdot\left(V_x^{\mathrm{ACS}}\cdot\sin\theta_l\cos\phi + V_z^{\mathrm{ACS}}\cos\theta_l\right).\end{aligned} \tag{A59}$$

Thus far, we have considered explicit expressions of the DFMR in the Keplerian and perturbed orbits. Another issue concerning the azimuthal resolution is the beam-crossing velocity. In the LBSAR, the beam-crossing velocity can be approximated by

$$V_g \approx \left\|\mathbf{V}_{\mathbf{TOI}} - R_{\mathrm{TOI}}\cdot\frac{\mathbf{V}_{\mathbf{SAR}}}{R_{\mathrm{SAR}}}\cdot\cos\beta\right\|_2. \tag{A60}$$

According to (A42) and (A43), we have

$$\cos\beta = \frac{R_{\mathrm{SAR}} - R_{\mathrm{ST}}\cos\theta_l}{R_{\mathrm{TOI}}}. \tag{A61}$$

Substituting (A61) into (A60), one can yield

$$V_g = \left\|\mathbf{V}_{\mathbf{TOI}} - \mathbf{V}_{\mathbf{SAR}}\cdot\frac{R_{\mathrm{SAR}} - R_{\mathrm{ST}}\cos\theta_l}{R_{\mathrm{SAR}}}\right\|_2. \tag{A62}$$

The TOI's linear velocity vector due to Earth's rotation can be obtained by substituting (A24) into (A19), as (A63), shown at the top of the page.

As a consequence, one arrives at the beam-crossing velocity in the Keplerian and perturbed orbits

$$V_g^{\mathrm{kep}} = \left\|\mathbf{V}_{\mathbf{TOI}}^{\mathbf{ACS}} - \mathbf{p}\cdot V_{\mathrm{kep}}\left(1 - R_{\mathrm{ST}}R_{\mathrm{SAR}}^{-1}\cos\theta_l\right)\right\|_2 \tag{A64}$$

$$V_g^{\mathrm{per}} = \left\|\mathbf{V}_{\mathbf{TOI}}^{\mathbf{ACS}} - \mathbf{V}_{\mathbf{SAR}}^{\mathbf{ACS}}\cdot\left(1 - R_{\mathrm{ST}}R_{\mathrm{SAR}}^{-1}\cos\theta_l\right)\right\|_2 \tag{A65}$$

where $\mathbf{p}$ and $\mathbf{V}_{\mathbf{SAR}}^{\mathbf{ACS}}$ are given in (A2a) and (A26), respectively.

REFERENCES

[1] J. B. Campbell, *Introduction to Remote Sensing*, 5th ed. New York, NY, USA: Guilford Press, 2010.

[2] M. D'Errico, *Distributed Space Missions for Earth System Monitoring*. New York, NY, USA: Springer, 2013.

[3] O. Dubovik et al., "Grand challenges in satellite remote sensing," *Frontiers Remote Sens.*, vol. 2, Feb. 2021, Art. no. 619818.

[4] S. J. Purkis and V. V. Klemas, *Remote Sensing and Global Environmental Change*. Chichester, U.K.: Wiley, 2011.

[5] A. Moussessian, C. Chen, W. Edelstein, S. Madsen, and P. Rosen, "System concepts and technologies for high orbit SAR," in *IEEE MTT-S Int. Microw. Symp. Dig.*, Jul. 2005, pp. 1623–1626.

[6] I. A. Crawford and K. H. Joy, "Lunar exploration: Opening a window into the history and evolution of the inner solar system," *Phil. Trans. Roy. Soc. A, Math., Phys. Eng. Sci.*, vol. 372, no. 2024, Sep. 2014, Art. no. 20130315.

[7] J. R. Johnson, P. G. Lucey, T. C. Stone, and M. I. Staid. *Visible/Near-Infrared Remote Sensing of Earth From the Moon*. Accessed: Sep. 11, 2018. [Online]. Available: http://www.lpi.usra.edu/meetings/LEA/whitepapers/Johnson_etal_v02.pdf

[8] M. Ramsey. *ESS Science Planning and Lunar Workshop Overview*. Accessed: Sep. 11, 2020. [Online]. Available: http://www.lpi.usra.edu/meetings/LEA/presentations/OpeningPlenary/Ramsey_ESS.pdf

[9] M. Ramsey. *ESS Findings: Lunar Science Planning and Workshop Overview*. Accessed: Mar. 2, 2018. [Online]. Available: https://www.lpi.usra.edu/meetings/LEA/presentations/closing_plenary/Ramsey_ESS_summary_20070302.pdf

[10] H. Guo, G. Liu, and Y. Ding, "Moon-based Earth observation: Scientific concept and potential applications," *Int. J. Digit. Earth*, vol. 11, no. 6, pp. 546–557, Jul. 2017.

[11] H. Ye, H. Guo, G. Liu, and Y. Ren, "Observation duration analysis for Earth surface features from a Moon-based platform," *Adv. Space Res.*, vol. 62, no. 2, pp. 274–287, 2018.

[12] I. A. Crawford et al., "Back to the Moon: The scientific rationale for resuming lunar surface exploration," *Planet. Space Sci.*, vol. 74, no. 1, pp. 3–14, Dec. 2012.

[13] W. Parks, V. Meadows, P. Mccullough, M. Postman, B. Bussey, and C. Christian, "Lunar based observations of the Earth as a planet," in *Proc. Astrobiol. Sci. Conf.*, League City, TX, USA, Apr. 2010, p. 98195.

[14] A. Renga, "Configurations and performance of Moon-based SAR systems for very high resolution Earth remote sensing," in *Proc. AIAA Pegasus Aerosp. Conf.*, Apr. 2007, pp. 12–13.

[15] A. Renga and A. Moccia, "Preliminary analysis of a moonbased interferometric SAR system for very high resolution Earth remote sensing," in *Proc. 9th ILEWG Int. Conf. Explor. Utilisation Moon*, pp. 22–26, Oct. 2007.

[16] A. Moccia and A. Renga, "Synthetic aperture radar for Earth observation from a lunar base: Performance and potential applications," *IEEE Trans. Aerosp. Electron. Syst.*, vol. 46, no. 3, pp. 1034–1051, Jul. 2010.

[17] Z. Xu, K.-S. Chen, G. Liu, and H. Guo, "Spatiotemporal coverage of a Moon-based synthetic aperture radar: Theoretical analyses and numerical simulations," *IEEE Trans. Geosci. Remote Sens.*, vol. 58, no. 12, pp. 8735–8750, Dec. 2020.

[18] G. Fornaro, G. Franceschetti, F. Lombardini, A. Mori, and M. Calamia, "Potentials and limitations of moon-borne SAR imaging," *IEEE Trans. Geosci. Remote Sens.*, vol. 48, no. 7, pp. 3009–3019, Jul. 2010.

[19] A. Renga and A. Moccia, "Moon-based synthetic aperture radar: Review and challenges," in *Proc. IEEE Int. Geosci. Remote Sens. Symp. (IGARSS)*, Jul. 2016, pp. 3708–3711.

[20] H. Guo, Y. Ding, G. Liu, D. W. Zhang, W. Fu, and L. Zhang, "Conceptual study of lunar-based SAR for global change monitoring," *Sci. China Earth Sci.*, vol. 57, pp. 1771–1779, Aug. 2014.

[21] Z. Xu and K. S. Chen, "On signal modeling of moon-based synthetic aperture radar (SAR) imaging of Earth," *Remote Sens.*, vol. 10, no. 3, p. 486, Mar. 2018.

[22] J. Dong et al., "An analysis of spatiotemporal baseline and effective spatial coverage for lunar-based SAR repeat-track interferometry," *IEEE J. Sel. Topics Appl. Earth Observ. Remote Sens.*, vol. 12, no. 9, pp. 3458–3469, Sep. 2019.

[23] Z. Xu and K.-S. Chen, "Effects of the Earth's curvature and lunar revolution on the imaging performance of the Moon-based synthetic aperture radar," *IEEE Trans. Geosci. Remote Sens.*, vol. 57, no. 8, pp. 5868–5882, Aug. 2019.

[24] Z. Xu, K.-S. Chen, and G. Zhou, "Effects of the Earth's irregular rotation on the moon-based synthetic aperture radar imaging," *IEEE Access*, vol. 7, pp. 155014–155027, 2019.
[25] Z. Xu, K.-S. Chen, and G. Zhou, "Zero-Doppler centroid steering for the moon-based synthetic aperture radar: A theoretical analysis," *IEEE Geosci. Remote Sens. Lett.*, vol. 17, no. 7, pp. 1208–1212, Jul. 2020.
[26] Z. Xu and K.-S. Chen, "Effects of the 'stop-and-go' approximation on the lunar-based SAR imaging," *IEEE Geosci. Remote Sens. Lett.*, vol. 19, pp. 1–5, 2022, doi: 10.1109/LGRS.2021.3070323.
[27] Z. Xu, K.-S. Chen, Z.-L. Li, and G.-Y. Du, "Apsidal precession effects on the lunar-based synthetic aperture radar imaging performance," *IEEE Geosci. Remote Sens. Lett.*, vol. 18, no. 6, pp. 1079–1083, Jun. 2021.
[28] Z. Xu, K.-S. Chen, and G. Liu, "On orbital determination of the lunar-based SAR under apsidal precession," *IEEE Trans. Geosci. Remote Sens.*, vol. 60, 2022, Art. no. 5228217, doi: 10.1109/TGRS.2022.3176836.
[29] Z. Xu, K.-S. Chen, and G. Liu, "On evaluating the imaging performance and orbital determination under perturbations of orbital inclination and RAAN in the lunar-based SAR," *IEEE Trans. Geosci. Remote Sens.*, vol. 60, 2022, Art. no. 5231519, doi: 10.1109/TGRS.2022.3188294.
[30] O. Montenbruck, E. Gill, and F. Lutze, *Satellite Orbits: Models, Methods, and Applications*. Berlin, Germany: Springer, 2002.
[31] M. Jiang, W. Hu, C. Ding, and G. Liu, "The effects of orbital perturbation on geosynchronous synthetic aperture radar imaging," *IEEE Geosci. Remote Sens. Lett.*, vol. 12, no. 5, pp. 1106–1110, May 2015.
[32] I. G. Cumming and F. H. Wong, *Digital Processing of Synthetic Aperture Radar Data: Algorithm and Implementation*. Norwood, MA, USA: Artech house, 2005.
[33] K. S. Chen, *Principles of Synthetic Aperture Radar: A System Simulation Approach*. Boca Raton, FL, USA: CRC Press, 2015.
[34] M. I. Skolnik, *Radar Handbook*, 3rd ed. New York, NY, USA: McGraw-Hill, 2008.
[35] H. Ye, H. Guo, G. Liu, J. Ping, and Q. Guo, "Impacts of platform's position errors on geolocation for a moon-based sensor," *IEEE Geosci. Remote Sens. Lett.*, vol. 17, no. 1, pp. 112–116, Jan. 2020.
[36] H. Ye, W. Zheng, H. Guo, and G. Liu, "Effects of temporal sampling interval on the moon-based Earth observation geometry," *IEEE J. Sel. Topics Appl. Earth Observ. Remote Sens.*, vol. 13, pp. 4016–4029, 2020.
[37] H. Ye, H. Guo, G. Liu, and Y. Ren, "Observation scope and spatial coverage analysis for Earth observation from a Moon-based platform," *Int. J. Remote Sens.*, vol. 39, pp. 5809–5833, Oct. 2017.
[38] W. M. Folkner, J. G. Williams, D. H. Boggs, R. S. Park, and P. Kuchynka, "The planetary and lunar ephemerides DE430 and DE431," *Interplanetary Netw. Progr. Rep.*, vol. 196, pp. 1–81, Feb. 2014.
[39] J. C. Curlander and R. N. McDonough, *Synthetic Aperture Radar*. New York, NY, USA: Wiley, 1991.
[40] S. J. Ostro, "Planetary radar astronomy," *Rev. Mod. Phys.*, vol. 65, no. 4, pp. 1235–1279, Oct. 1993.
[41] J. L. H. Webb, D. C. Munson, and N. J. S. Stacy, "High-resolution planetary imaging via spotlight-mode synthetic aperture radar," *IEEE Trans. Image Process.*, vol. 7, no. 11, pp. 1571–1582, Nov. 1998.

Zhen Xu (Member, IEEE) received the Ph.D. degree from the University of Chinese Academy of Sciences (UCAS), Beijing, China, and the Institute of Remote Sensing and Digital Earth, Chinese Academy of Sciences, Beijing, in 2020.

He joined the Department of Electronic and Information Engineering and the Guangdong Provincial Key Laboratory of Digital Signal and Image Processing, Shantou University, Shantou, Guangdong, China, in 2020. His research interests include the synthetic aperture radar (SAR) system design and signal processing, particularly the lunar-based SAR (LBSAR) and the perturbation & atmospheric effects on high-orbit SAR imaging.

Dr. Xu received the Young Scientist Award from the International Conference on Space, Aeronautical, and Navigational Electronics in 2018. He was awarded the ZhuLi Yuehua Excellent Doctoral Student Scholarship and Outstanding Graduates of UCAS, the Excellent Graduates of High Education in Beijing City, the Outstanding Talent of Shantou University, and the High-Level Talent of Shantou City in 2020.

Kun-Shan Chen (Fellow, IEEE) received the Ph.D. degree in electrical engineering from The University of Texas at Arlington, Arlington, TX, USA, in 1990.

From 1992 to 2014, he was a Professor with National Central University, Taoyuan City, Taiwan. From 2014 to 2019, he was with the Institute of Remote Sensing and Digital Earth, Chinese Academy of Sciences, Beijing, China. Since 2019, he has been a National Distinguished Professor with the Guilin University of Technology, Guilin, China. He has authored or coauthored over 400 referred journal articles and conference papers, and contributed ten book chapters. He is a coauthor (with A. K. Fung) of *Microwave Scattering and Emission Models for Users* (Artech House, 2010), the author of *Principles of Synthetic Aperture Radar (SAR): A System Simulation Approach* (CRC Press, 2015) and *Radar Scattering and Imaging of Rough Surface: Modeling and Applications With MATLAB* (CRC Press, 2020), and a coeditor (with X. Li, H. Guo, and X. Yang) of *Advances in SAR Remote Sensing of Ocean* (CRC Press, FL, USA, 2018). His research interests include microwave remote sensing theory, modeling, systems, and measurement, and intelligent signal processing and data analytics for radar.

Dr. Chen is a member of the Academia Europaea. He has served as a member of the Editorial Board of the PROCEEDINGS OF THE IEEE from 2014 to 2019. He has been a member of the Editorial Board of IEEE ACCESS since 2020. He was an IEEE GRSS Adcom Member from 2010 to 2014. He received the 2021 IEEE GRSS Fawwaz Ulaby Distinguished Achievement Award for his contributions to microwave scattering and emission modeling of a rough surface and radar image simulation and understanding. He was the Founding Chair of the GRSS Taipei Chapter. He was the Co-Chair of the Technical Committee for International Geoscience and Remote Sensing Symposium (IGARSS) 2016, IGARSS 2017, and IGARSS 2020. His academic activities include being an Associate Editor of the IEEE TRANSACTIONS ON GEOSCIENCE AND REMOTE SENSING since 2000, a Guest Editor of the IEEE TRANSACTIONS ON GEOSCIENCE AND REMOTE SENSING Special Issue on Remote Sensing for Major Disaster Prevention, Monitoring and Assessment in 2007, the Founding Deputy Editor-in-Chief of IEEE JOURNAL OF SELECTED TOPICS IN APPLIED EARTH OBSERVATIONS AND REMOTE SENSING from 2008 to 2010, and a Guest Editor of the PROCEEDINGS OF THE IEEE Special Issue on Remote Sensing for Natural Disaster in 2012. He has also served as a Guest Editor for the Special Issue on Data Restoration and Denoising of Remote Sensing Data and the Special Issue on Radar Imaging Theory, Techniques, and Applications, both for *Remote Sensing*.

Huadong Guo (Member, IEEE) received the Graduation degree from the Geology Department, Nanjing University, Nanjing, China, in 1977, and the M.Sc. degree in cartography and geographical information system from the Graduate University of the Chinese Academy of Sciences (CAS), Beijing, China, in 1981.

He is currently the Academician of CAS, the Foreign Academician of the Russian Academy of Sciences, Moscow, Russia, and the Finland Academy of Science and Humanities, Helsinki, Finland, and the Academician of the Academy of Sciences of developing countries and the International Academy of Sciences of Eurasia. He was the project leader of more than ten key programs related to Earth observation and is the Principal Investigator for SIR-C/X-SAR, JERS-1 SAR, ERS-1/2 SAR, Radarsat-1/2, ENVISAT, SRTM, and ALOS programs. He has authored or coauthored more than 200 Science Citation Index (SCI) index papers and 16 books.

Prof. Guo was a recipient of three national awards in science and technology and nine awards from the Chinese Academy of Sciences. He is the President of the International Digital Earth Society, the Chair of the International Environmental Remote Sensing Committee, a member of the Expert Group of the United Nations Technical Promotion Mechanism for Sustainable Development Goals (SDGs), the Director of the International Centre for Space Technology for Natural and Cultural Heritage of United Nations Educational Scientific and Cultural Organization (UNESCO), and an Editor of *International Journal of Digital Earth* and *International Journal of Big Earth Data*.